# CellGeo: A computational platform for the analysis of shape changes in cells with complex geometries

Denis Tsygankov,[1] Colleen G. Bilancia,[2] Eric A. Vitriol,[4] Klaus M. Hahn,[1,3] Mark Peifer,[2,3] and Timothy C. Elston[1]

[1]Department of Pharmacology, [2]Department of Biology, and [3]Lineberger Comprehensive Cancer Center, University of North Carolina at Chapel Hill, Chapel Hill, NC 27599
[4]Department of Cell Biology, Emory University, Atlanta, GA 30322

Cell biologists increasingly rely on computer-aided image analysis, allowing them to collect precise, unbiased quantitative results. However, despite great progress in image processing and computer vision, current computational approaches fail to address many key aspects of cell behavior, including the cell protrusions that guide cell migration and drive morphogenesis. We developed the open source MATLAB application CellGeo, a user-friendly computational platform to allow simultaneous, automated tracking and analysis of dynamic changes in cell shape, including protrusions ranging from filopodia to lamellipodia. Our method maps an arbitrary cell shape onto a tree graph that, unlike traditional skeletonization algorithms, preserves complex boundary features. CellGeo allows rigorous but flexible definition and accurate automated detection and tracking of geometric features of interest. We demonstrate CellGeo's utility by deriving new insights into (a) the roles of Diaphanous, Enabled, and Capping protein in regulating filopodia and lamellipodia dynamics in *Drosophila melanogaster* cells and (b) the dynamic properties of growth cones in catecholaminergic α–differentiated neuroblastoma cells.

## Introduction

Cell protrusions are an essential driver of dynamic cell shape changes and motility during development and disease. Morphogenic processes from gastrulation to organogenesis require coordinated protrusive behavior to shape tissues and organs. Cell protrusions are also essential for cell migration during wound healing, and cancer cells use protrusions to migrate from primary tumors during metastasis. Cells use both lamellipodia and filopodia to generate shape changes and drive motility, making it imperative to understand how the dynamics of both structures are regulated.

Recent advances in live-cell imaging, including new microscope designs and novel molecular probes, allowed biologists to visualize cellular behavior with extraordinary precision and detail. However, to fully take advantage of these advances requires novel computational methods for image processing and analysis (Meijering et al., 2004; Costantino et al., 2008; Fanti et al., 2011). Here, we present the computational platform CellGeo, a MATLAB application to identify, track, and characterize dynamic cell shape changes (Fig. 1 A). The key step in

CellGeo is the representation of any arbitrary cell shape as a tree graph (Fig. 1, C–F; and Video 1). This conversion facilitates precise definitions of shape features, such as filopodia and lamellipodia, and quantitative analyses of their dynamics. CellGeo is a fully automated system with a graphical user interface (GUI) for easy adjustment of parameters for flexible and accurate protrusion and cell body detection and analysis of any cell type (Fig. 1 A). CellGeo has an intuitive/self-explanatory design that allows two modes of operation: (1) an interactive exploratory mode, in which users can see how changes in parameters affect the analysis and adjust them accordingly; and (2) an unsupervised production mode, in which users simply import data, click a button, and save results using default or previously set parameter values.

To demonstrate CellGeo's utility, we use the platform to analyze the effects of the actin regulators Diaphanous (Dia), Enabled (Ena), and Capping protein (CP) on both filopodial and lamellipodial dynamics in *Drosophila melanogaster* cells (Fig. 1 B). Ena and Dia both localize to filopodia and lamellipodia, and overexpressing either drives both types of protrusions. However,
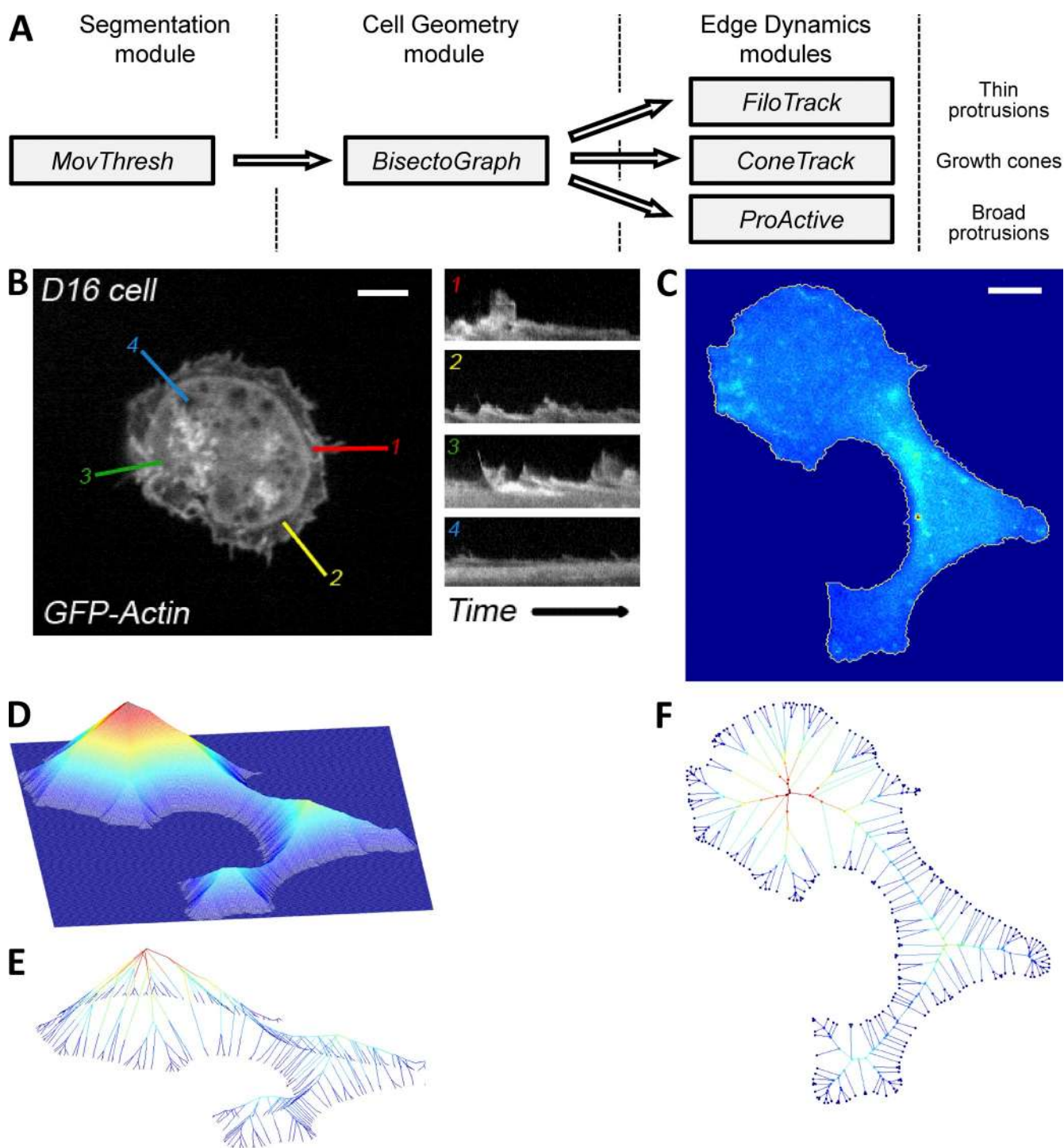
Figure 1. **CellGeo platform architecture and qualitative interpretation of the MAT.** (A) CellGeo package pipeline for defining, detecting and tracking both thin or broad cellular protrusions or growth cones. (B) *Drosophila* D16C3 cell expressing GFP-actin with four kymographs labeled 1–4 show high variability of protrusiveness within a single cell, making analysis biased by placement. Bar, 5 µm. (C) A cell and its boundary (yellow). Bar, 10 µm. (D) Distance function $F(x, y)$, which measures the minimum distance from each point $(x, y)$ inside the cell to the cell boundary. (E) Ridges (surface discontinuities) of the minimum distance function in D. (F) Medial axis as a top view of the ridges in E.

only Ena is required for filopodia number and length, demonstrating that CellGeo can identify distinct roles of similar actin regulators in controlling the complex composition of cell protrusions (Videos 2–6). We also find Ena and Dia can act independently of one another in the formation of filopodia and broad protrusions and that CP is required to limit Ena activity, likely

by limiting availability of barbed ends. To further demonstrate CellGeo's versatility, we use it to study neuronal growth cone dynamics and the role of the GTPase RhoA (Etienne-Manneville and Hall, 2002; Jaffe and Hall, 2005) in driving this behavior. Our analysis revealed in a quantitative way the spatiotemporal distribution of RhoA activity in growth cones and cell bodies

during growth cone protrusion and retraction. Our analysis also revealed unexpected correlations between geometric characteristics of growth cones and the delay in onset of growth cone retraction after treatment with lysophosphatidic acid (LPA).

## Results

### Defining cell edge features

The complex structure and dynamics of cellular protrusions reflects their functional diversity, making designing automated algorithms for quantifying their behavior challenging. We developed a novel approach for identifying and tracking protrusions that functions reliably even in the presence of irregular geometries and complex dynamics.

Our method begins by identifying the cell boundary in each frame of a time-lapse video. Although other commonly used software packages like ImageJ or MetaMorph provide segmentation routines, we included a simple segmentation module, MovThresh, to incorporate additional features for dynamic shape analysis and make CellGeo a stand-alone platform. MovThresh automatically thresholds each frame of a video using the Otsu algorithm or one of the other built-in segmentation routines, overlays the detected boundary with the original image, and displays suggested threshold values as a function of time (Fig. S1). If the algorithm accurately captured the cell edge in each frame, no additional steps are required. Often, however, the threshold values determined by the algorithm vary from frame to frame. Therefore, depending on the type of analysis to be performed, users might opt to use a smooth curve through the suggested threshold values or a constant (e.g., mean) value to rethreshold all frames consistently. In special cases, when image brightness significantly changes during the experiment (e.g., induction of a fluorescent protein) users can interactively set the threshold in a way appropriate for the current analysis. The main purpose of these steps is to avoid or minimize boundary artifacts, such as unresolved or merged filopodia, that result from over- or under-thresholding images (Fig. 2, A–C).

The output of MovThresh is a closed polygon made from lines connecting the centers of neighboring boundary pixels (Fig. S2). In addition to being computationally efficient and simple, this representation preserves the pixelated nature of the raw data and does not require any image preprocessing. Importantly, the next CellGeo module, BisectoGraph, is based on a grid-free approach so that no association with pixel centers is necessary: BisectoGraph can process any simple closed polygon specified by (x, y) coordinates.

BisectoGraph is the key step in analyzing cell edge dynamics: it creates a representation of the entire cell that makes quantifying protrusions and cell body dynamics precise and unbiased. BisectoGraph relies on a Voronoi transformation that converts the cell boundary found by MovThresh into a tree graph. Voronoi diagrams were originally introduced as a way to partition space into regions that uniquely enclose individual points of an arbitrary discrete set (Aurenhammer, 1991). However, the Voronoi transformation also can be applied to a discrete set of line segments or, as a limiting case, to a closed polygon. The Voronoi diagram inside a polygon is a union of the medial axis and a set of rays originating at concave boundary points (Materials and methods; Fig. S4; Mayya and Rijan, 1995).

The concept of the medial axis transform (MAT; or symmetric axis or skeleton) was introduced by Blum (1967) as a method for cell shape analysis. The MAT of a plane shape is defined as the set formed from the union of the centers of all maximal inscribed circles (circles contained within the shape that share at least two boundary points with it; Chin et al., 1999). For example, the MAT of a rectangle consists of five branches (Fig. 3 A). Since its introduction, the MAT found applications in many areas, including object recognition, graphics, 3D modeling, computer-aided manufacturing, and characterizing structures of proteins or organs (Morse et al., 1994; Styner et al., 2003; Abeysinghe et al., 2008).

A common theme in all these applications is the generation of a reduced representation of the shape of interest that captures its large-scale features. Therefore, algorithms for constructing MATs are typically accompanied by pruning algorithms that decide which medial axis branches can safely be removed (Tek and Kimia, 2003; Aichholzer et al., 2009). A major shortcoming of this is that small perturbations to shape can generate disproportionately large perturbations to the MAT, necessitating postprocessing to reduce the effects of noise. In contrast, we demonstrate that for the analysis of protrusion dynamics, it is useful to keep the complete Voronoi tree graph with branches reaching every boundary point and define boundary measures that are insensitive to noise (Materials and methods). Fig. 2 illustrates the fact that although small (less than 1 pixel) boundary perturbations produce significant differences in the tree graph (Fig. 2 D, white and black lines), the detection of protrusion tips using these graphs by means of the boundary profile is not significantly affected. Indeed, Fig. 2 (E–G) shows 100 overlaid boundaries and the detected tips for each boundary (Fig. 2, E–G, red dots), whereas Fig. 2 (H–J) shows the resulting boundary profiles and the local maxima corresponding to the tips (Fig. 2, H–J, also marked by red dots).

To illustrate the effect of small perturbations, consider a digital image of an inclined rectangle (Fig. 3 B). If the goal is to have the computer recognize the shape as a rectangle, pruning all branches that appeared as a result of pixelation is essential. However, in live-cell imaging, this pruning is not only unnecessary but also undesirable. The complexity of the MAT in Fig. 3 D accurately captures the complexity of the cell shape in Fig. 3 C, where boundary features at all scales are of interest. Thus, the high sensitivity of MATs to small-scale features on the boundary gives our algorithm high accuracy and efficiency for protrusion identification, tracking, and quantification.

The MAT generates a tree graph that emanates from a single root at the cell center, with each branch ending at a unique convex point on the cell boundary (Fig. 3 D). To complete the boundary profile, we extend the MAT to the Voronoi graph to include concave boundary points as well (Fig. S2 F and Fig. S4). With this representation, the distance from the cell center to any boundary point can be measured along a path inside the cell. This feature turns out to be very powerful for analyzing cell shape dynamics because the tips of each protrusion can be easily identified as local maxima when the path distance is plotted
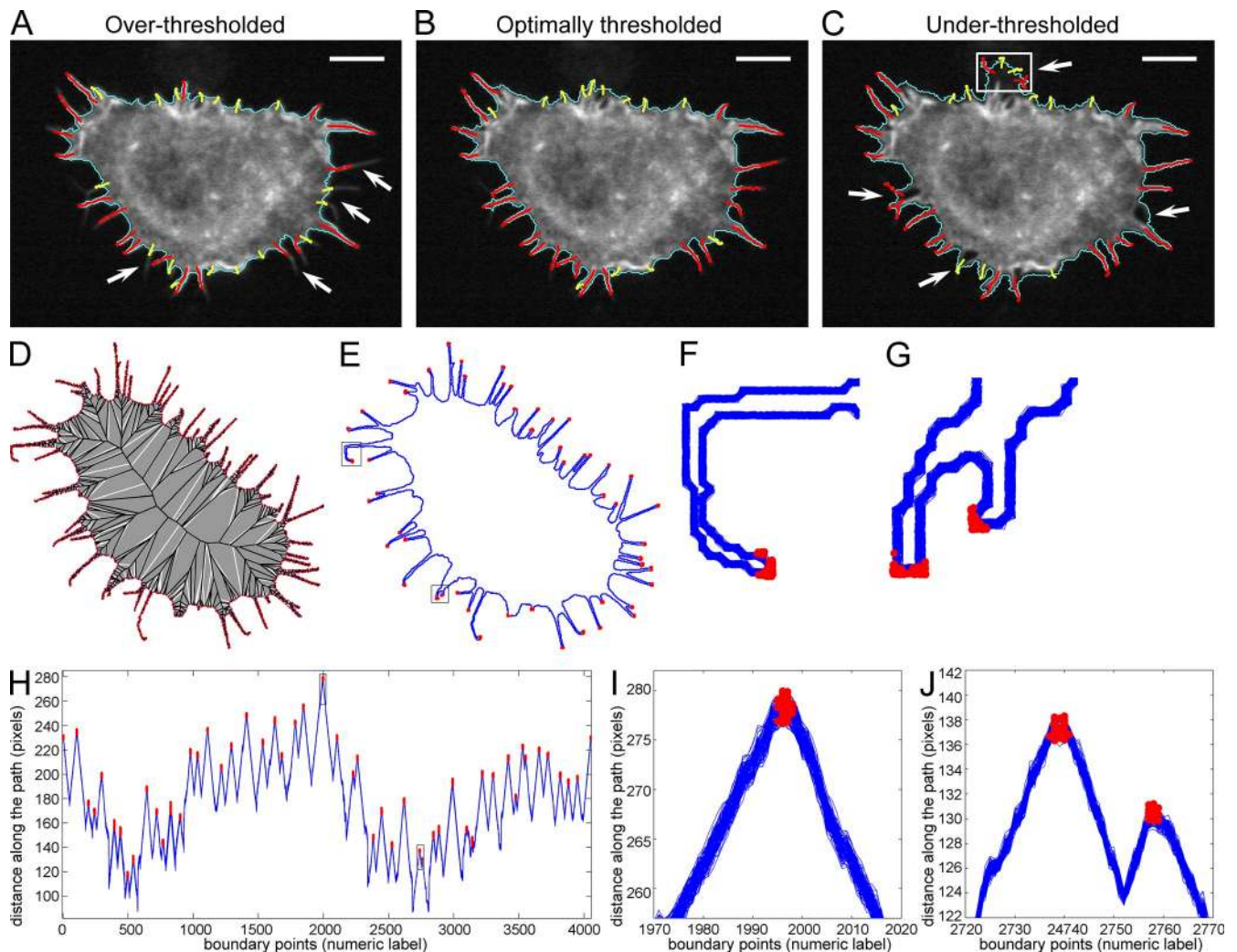
Figure 2. **Boundary artifacts and sensitivity to small boundary perturbations.** (A–C) The same cell image with the boundary (cyan) identified at three different threshold values. Bars, 5 µm. (A) Overthresholded case, in which thin filopodia (white arrows) are not properly resolved. Red and yellow lines in A–C indicate central lines (skeletons) of protrusions that are longer and shorter than the critical length $L_{cr}$, respectively. (B) Optimally thresholded case, in which all boundary features are properly captured. (C) Underthresholded case, in which filopodia start to merge (white arrows) and a small region of background noise (white rectangle) becomes a part of the misrepresented cell boundary. In all cases, FiloTrack identifies and tracks filopodia for a given boundary representation, but improperly captured cell features may reduce the accuracy of the final statistics. MovThresh is designed to find optimal thresholds and minimize possible boundary artifacts. (D) Two overlaid MATs (black and white) show small perturbation in cell boundaries can cause significant differences in the tree graph. Random noise (<1-pixel length) creates significant differences in the location of the graph edges and their number so that direct comparison of two MATs is problematic. (E) Rather than comparing MATs directly, we use extracted boundary profiles. This illustrates 100 overlaid boundaries that were perturbed within 1-pixel size. Red dots show protrusion tips on each boundary as determined by the corresponding boundary profiles (H). Boundary profiles are similar despite differences in tree graphs. (F and G) Expanded views of two regions highlighted in E. The spread of the detected protrusion tips (red) is on the same scale as the boundary perturbations, showing that small perturbations do not drastically change protrusion identification when using the boundary profiles. (H) 100 overlaid boundary profiles of perturbed cell outlines. Red dots show local maxima of the profiles. (I and J) Expanded views of two regions highlighted in H and corresponding to the protrusions shown in F and G. Hypersensitivity of the MAT to the boundary perturbation does not translate into hypersensitivity of protrusion tip detection using the boundary profiles, even though the latter are created using the MAT.

as a function of the boundary points (Fig. 3 E). Because protrusions can have very different geometries (shape, length, area, etc.), another advantage of our approach is that it always identifies a unique reference point, the protrusion tip. Fig. 4 demonstrates the accuracy of the Voronoi graph for a cell with many protrusions.

BisectoGraph allows users to import boundaries identified in MovThresh or extract them automatically from masks in a TIFF stack file. Users can batch process many video files or single frames in a convenient way by specifying file locations and

numbering in the folder hierarchy. After loading, each boundary is regularized to eliminate self-crossings and degeneracies (Materials and methods; Fig. S2, D and E; and Fig. S3). Users have the option to explore graph structure, resulting boundary profiles of the cell, and the length–width relationship of each identified protrusion (Fig. S5 A). By interactively specifying a critical width for filopodia, users can define the cell body (i.e., filopodia-free part of the cell), which can be analyzed in the fourth module of the CellGeo, ProActive, which is described in the section below on broad protrusions.
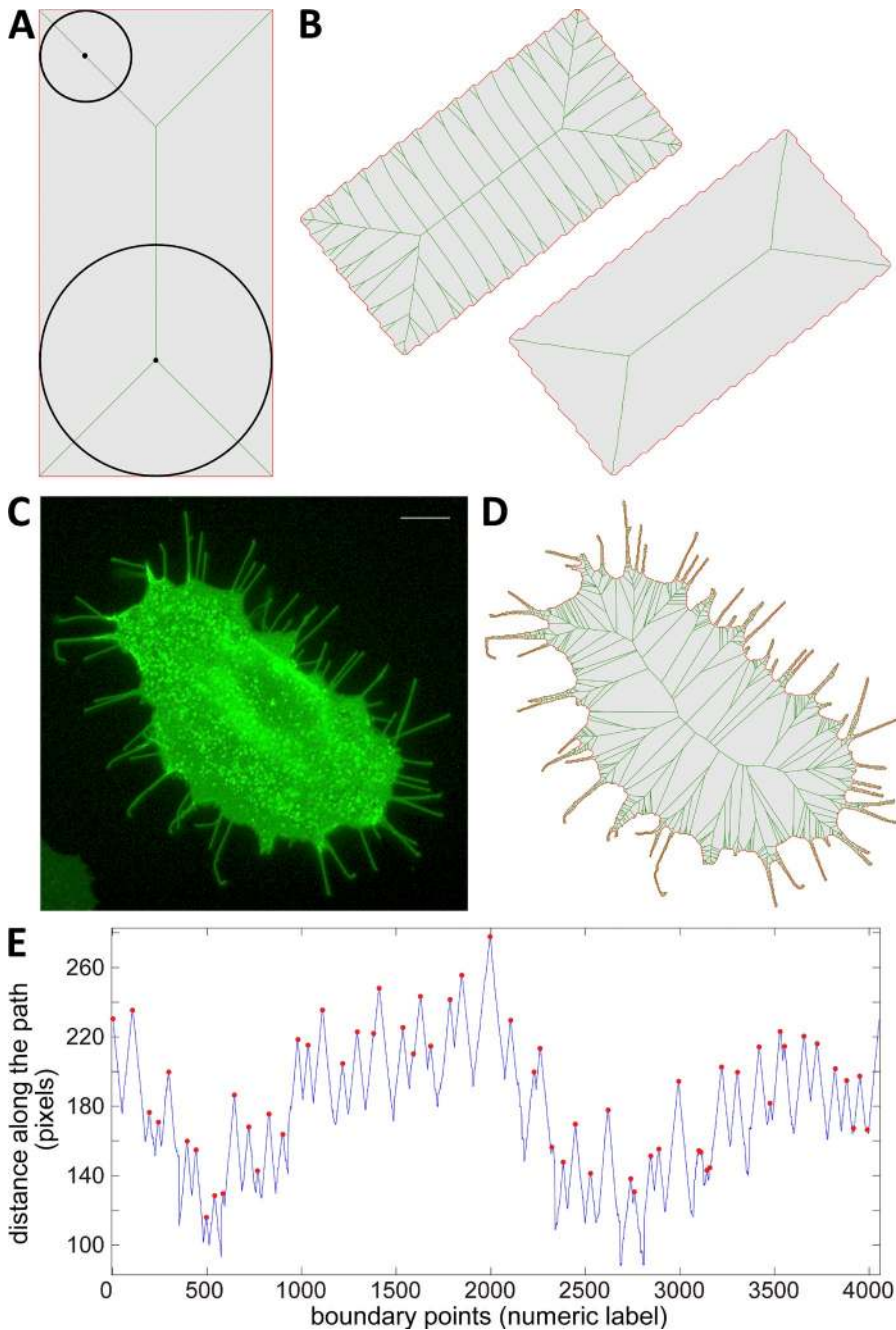
Figure 3. **Using the MAT to identify protrusions.** (A) MAT (green) of a rectangle (red). The black circles demonstrate that each point of MAT is the center of a circle that touches the boundary at two or more points. (B, left) A tilted rectangle on a discrete grid becomes pixelated, creating perturbations along the boundary resulting in a complex MAT. Typically, to reduce large effects of small boundary perturbations, pruning algorithms are used to remove unnecessary lines, leaving only the simple skeleton. (C) Cell with many protrusions presents a highly complex shape. Bar, 20 μm. (D) MAT of the boundary of the cell in C. In this case, the complexity of the MAT properly represents the complexity of cell shape. (E) Boundary profile of cell in C using the distance measured along the paths of the tree graph in D. Red dots at local maxima correspond to tips of cell protrusions.

## Defining and detecting filopodia-like protrusions

To define, track, and quantify filopodia, we use a very convenient feature of the MAT: each point of the graph is the center of a circle that is tangent to at least two boundary edges (Fig. 4 A). The radius of this circle, $R$, is equal to the shortest distances from the graph to the boundary. The tangent circle with the center at the root of the graph and radius $R_{max}$ is the largest possible circle that can be inscribed in the cell. These properties allow us to define geometric scales for cell protrusions. To see this, consider the distance $L$ from the tip of a protrusion to any point along the medial path (the path ending at the graph root). The function $R(L)$ is the radius of the inscribed circle at distance $L$

and is defined on the interval $(0, L_{path})$, in which $L_{path}$ is the total length of the path. Thus, $R(0) = 0$ and $R(L_{path}) = R_{max}$.

We can define a critical radius $R_{cr} < R_{max}$, which determines the maximum width of a filopodium (Fig. 4). Using this cutoff value, the protrusion length, $L_{pr}$, is found from the relation

$$R\left(L_{pr}\right) = R_{cr}. \qquad (1)$$

Using only this criterion, it is possible for the protrusion length to be smaller than its width at the base (i.e., $L_{pr} < R_{cr}$). Thus, to ensure only long, thin structures are identified as filopodia, we define a minimum length $L_{cr} \geq R_{cr}$ and require $L_{pr} > L_{cr}$. Thus, a pair of parameters $(R_{cr}, L_{cr})$ precisely defines a filopodium.
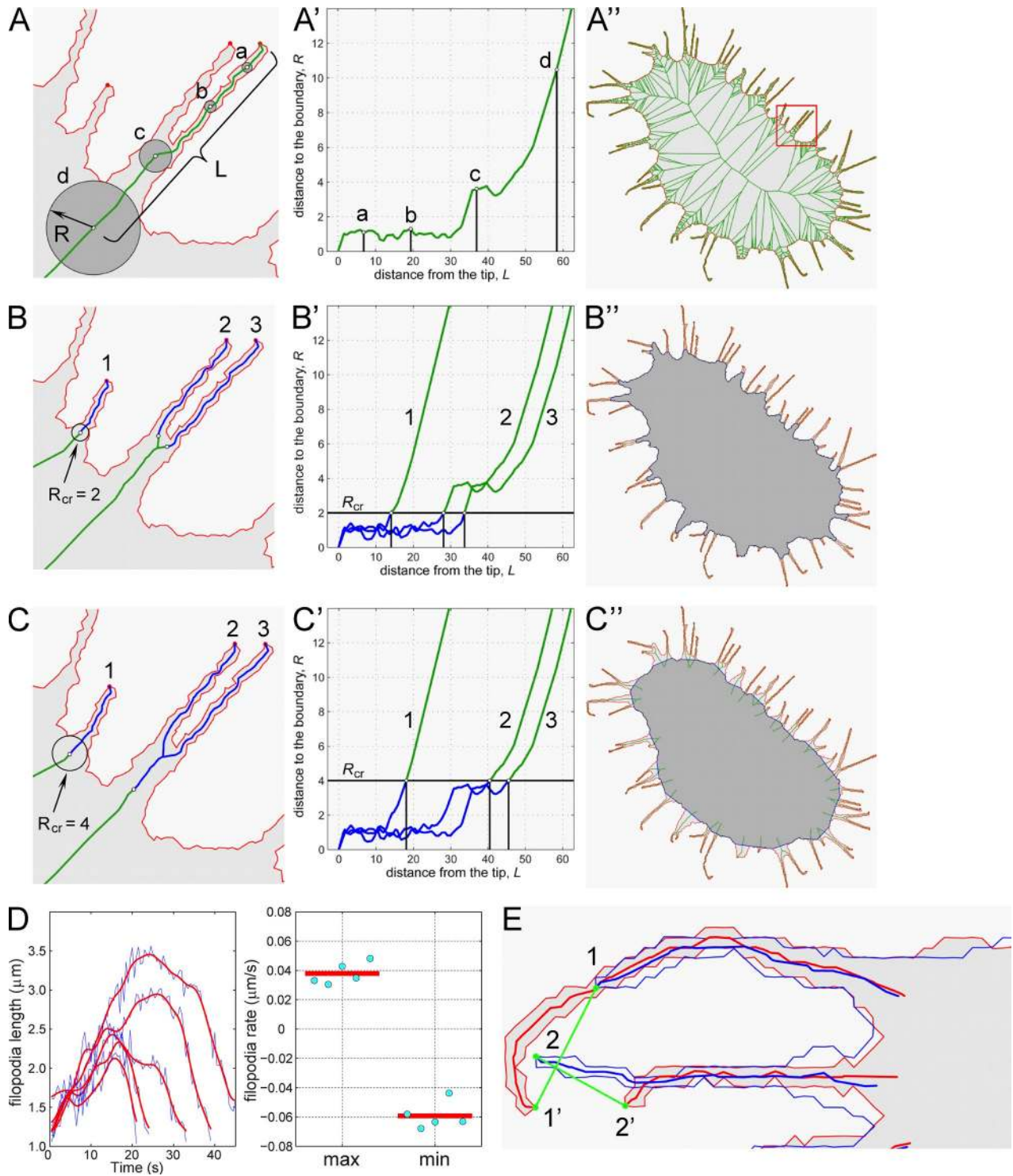
Figure 4. **Filopodia detection and tracking.** (A) Four inscribed circles (a, b, c, and d) with centers on a filopodium skeleton (green). The radius $R$ and distance $L$ from tip to center along the skeleton are labeled for the largest circle (d). (A') The shortest distance to the boundary $R$ as a function of the distance from the tip $L$. Vertical lines (a, b, c, and d) correspond to the circles in A. (A") An example of a cell outline (red) and corresponding MAT (green). The red box corresponds to the view in A, B, and C. (B and C) Filopodia skeletons (blue, 1, 2, and 3) satisfying a critical radius of 2 or 4 pixels, respectively. (B' and C') $R(L)$ curves for medial paths in B and C, respectively. Points where the line for $R_{cr}$ intersects with $R(L)$ curves define filopodia bases. (B" and C") Resulting filopodia and cell body mapping of the same cell using two different critical radii $R_{cr}$: 2.5 (B") and 7.5 (C"). (D) An example of protrusion and retraction rate analysis for the cell in Video 2. (left) The length of five of the tracked filopodia as a function of time (blue) and corresponding smoothed curves (red). Only filopodia that went through the full cycle of protruding and retracting are chosen for analysis. (right) Maximal and minimal velocities of filopodia (cyan dots) and corresponding mean values (red lines) calculated using smooth curves in the left graph. (E) The parameter $D$ is a measure of the distance between detected filopodium at time $t$ (blue) and $t + 1$ (red). If the change in position of two filopodia in consecutive frames is less than $D_{cr}$, they are considered the same filopodium. In this example, tracking only filopodia tips would fail to correctly track filopodia in time. However, FiloTrack correctly associates the tips 1' with 1 and 2' with 2 (green lines) because $D$ is computed using the skeletons, not just tips.

We use the term filopodium skeleton for the fragment of the medial path that satisfies these two criteria (Fig. 4, A–C″).

The critical radius and minimum length are both adjustable parameters in FiloTrack providing built-in flexibility in defining filopodia. This allows users to customize the definition of filopodia to the cell type and analysis to be performed. For example, setting a small critical radius captures only very thin filopodia (Fig. 4, B and B′), whereas a large critical radius incorporates wider protrusions (Fig. 4, C and C′). Likewise, adjusting the minimum length defines the threshold for identifying filopodia. Scroll bars allow users to quickly and easily set different combinations of critical radius and minimum length to precisely identify filopodia in any cell type (Fig. 5 A). FiloTrack automatically corrects for cases when filopodium skeletons overlap or when they become wider than the critical width at several places along their skeletons (Materials and methods).

### Tracking filopodia over time

FiloTrack allows users to easily quantify filopodia dynamics, measuring length, number, and lifetime. Because FiloTrack tracks filopodia over time, it also can compute protrusion and retraction rates (Fig. 4 D). Our tracking algorithm is based on pairing filopodia from consecutive video frames that are close to each other. However, the key feature of our approach is that the measure of distance between filopodia is not solely based on their tips but on their skeletons (Materials and methods). Thus, even when filopodia are too dynamic to make accurate frame to frame associations based solely on their tips, FiloTrack still accurately tracks them (Fig. 4 E). The critical distance, $D_{cr}$, defining how far a filopodium's position may shift between frames and still be identified as the same protrusion, is an adjustable parameter in FiloTrack (Fig. 5 B).

**Gap filling.** When analyzing videos, filopodia may temporarily go out of focus or transiently disappear as a result of other sources of noise. In these cases, the tracking algorithm would record two different filopodia with short lifetimes instead of one long-lived filopodia. Well-resolved filopodia might also temporarily dip below the critical length $L_{cr}$, and the algorithm would treat the reappearing filopodium as a new structure. If such events are frequent, statistical measurements will be biased toward a high mean filopodia number and short lifetimes.

FiloTrack was designed to resolve these issues. Once all pairs of filopodia from time points $t$ and $t + 1$ are found, unpaired filopodia at time $t + 1$ are compared with filopodia at time $t − 1$, identifying all filopodia that "blinked" for one time step. If unpaired filopodia remain, they are compared with filopodia at time $t − 2$. The procedure is continued until all time intervals up to a user-defined time gap, $G_{cr}$, are tested. Remaining unpaired filopodia are considered distinct structures, and the algorithm proceeds to the next time frame. The value of the maximum time gap $G_{cr}$ can be defined based on biological considerations. In most cases, $G_{cr}$ set at one to two frames was sufficient to eliminate the blinking effect without overestimating filopodia lifetime.

Important features of the GUI are that timelines of all tracked filopodia are displayed simultaneously on one graph (Fig. 5 B, right), and every gap event is indicated as an empty circle on the timeline. This provides a quick and easy way to assess the quality of the tracking and frequency of gaps. A large number of gaps might indicate that either protrusions change significantly on a time scale faster than the recording frame rate or that the filopodia detection or tracking parameters need to be adjusted.

**Lifetime filter.** The last parameter built into FiloTrack sets the minimum number of frames a filopodium must be present for it to be considered for analysis. The parameter $T_{cr}$ may be set to 0, and all tracked filopodia will be included. However, in many cases, users may choose to only track filopodia with a lifetime greater than a specified value.

FiloTrack allows easy adjustment of the parameters ($D_{cr}$, $G_{cr}$, and $T_{cr}$), so filopodia of any cell type are accurately tracked and analyzed (Fig. 4 E, Fig. 5 B, and Video 2). The output of FiloTrack includes mean number of filopodia at each time frame, number of tracked filopodia, mean filopodial length at each time frame, mean length of tracked filopodia, lifetime of tracked filopodia, and SDs from these means. In addition, the time dependence of the length of all tracked filopodia is saved and can be used to calculate the protrusion and retraction rates (Fig. 4 D).

### Quantifying the shape and dynamics of broad protrusions

Lamellipodial size and shape varies greatly between cell types: e.g., fish keratocytes have a very large, stable lamellipodium encompassing much of the cell, whereas lamellipodia at the leading edge of migrating epithelial cells during *Drosophila* dorsal closure are smaller and more dynamic. Additionally, cells may produce a mixture of filopodia and lamellipodia, using distinct suites of actin regulators. Precise tracking and quantification of all types of protrusion dynamics simultaneously in normal, diseased, or genetically manipulated cells is required to tease out the protein networks coordinating cell protrusive behaviors.

To assess the dynamics of broad protrusions, we again use a convenient feature of the Voronoi graph. Every filopodium consists of boundary points whose medial paths go through the filopodium base. Thus, the remainder of the cell is identified simply by excluding these points. This procedure provides a computationally straightforward method for partitioning the cell into two parts: filopodia and cell body (Fig. 6, A–C). This partitioning allows the dynamics of broad protrusions to be studied in parallel with filopodial dynamics.

After removing filopodia, we assess frame to frame changes in the remaining cell boundary (Fig. 6, D and D′). The cell boundary at time $t$ (Fig. 6, D and D′, blue) is overlaid with the cell boundary at time $t + 1$ (Fig. 6, D and D′, red). Then, the boundary at time $t + 1$ is compared with that at time $t + 2$ and so on, providing a time-lapse video of cell body dynamics (Videos 5 and 6). Changes in the boundary are colored white for areas of protrusion and black for areas of retraction (Fig. 6, D and D′).

The ProActive module allows users to display and quantify protrusion, retraction, or total activity and normalizes results to the cell perimeter or total cell area to distinguish protrusive activity from changes in total cell area (Fig. 6, E–G′). The default in ProActive is to compare successive video frames,
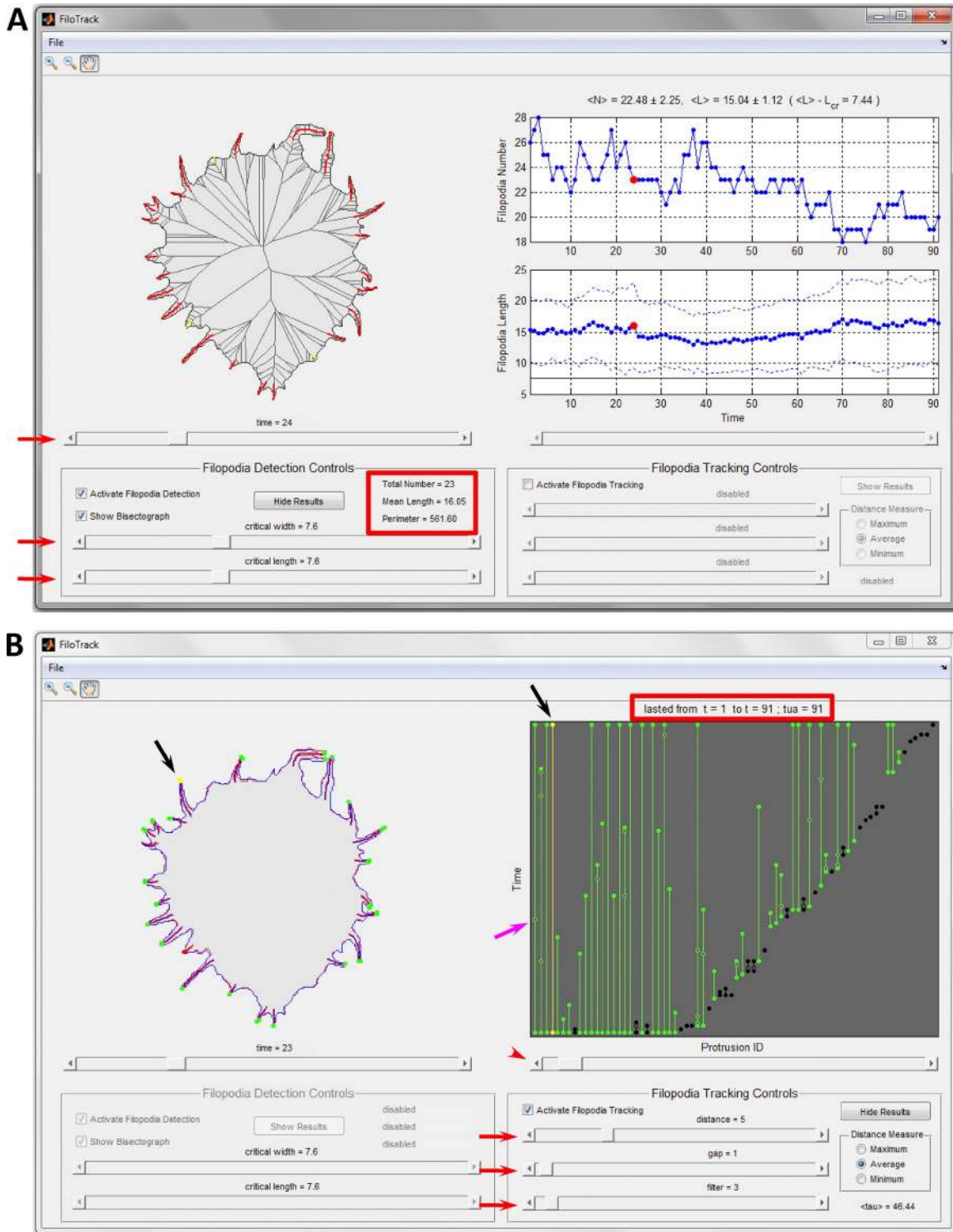
Figure 5. **FiloTrack module for detecting and tracking filopodia.** (A and B) Screenshots of GUI. The GUI contains a view of the cell, analysis results, and control panels for adjusting parameters and viewing results. (A) Filopodia detection. Cell data from BisectoGraph are loaded using the File menu, and the cell boundary appears in the cell view section (top left). Checking Show BisectoGraph and Activate Filopodia Detection displays the cell MAT and identified filopodia. Red arrows point to scroll bars to select movie frame (top), critical width (middle), and critical length (bottom). Filopodia meeting specified values of $R_{cr}$ and $L_{cr}$ are shown in red. Protrusions not meeting these criteria are shown in yellow. The number of protrusions, mean length, and cell perimeter for the current frame are highlighted by the red box. The Show Results button loads results for all time frames to the results section (top right) where filopodia number (top subsection) and mean length ± SD (bottom subsection) are shown. (B) Filopodia tracking. Clicking Activate Filopodia Tracking and Show Results changes the results section to show all time lines of the detected filopodia (vertical green lines). The magenta arrow marks one of the empty circles indicating temporal gaps in filopodia tracks. The red arrowhead indicates the scroll bar to select a single filopodium (yellow line in results section and yellow dots in cell view [black arrows]). The red box highlights lifetime information for the selected filopodium. Red arrows point to scroll bars for easily changing distance, gap filling, and lifetime filter parameters, with cell view and results sections updating accordingly.
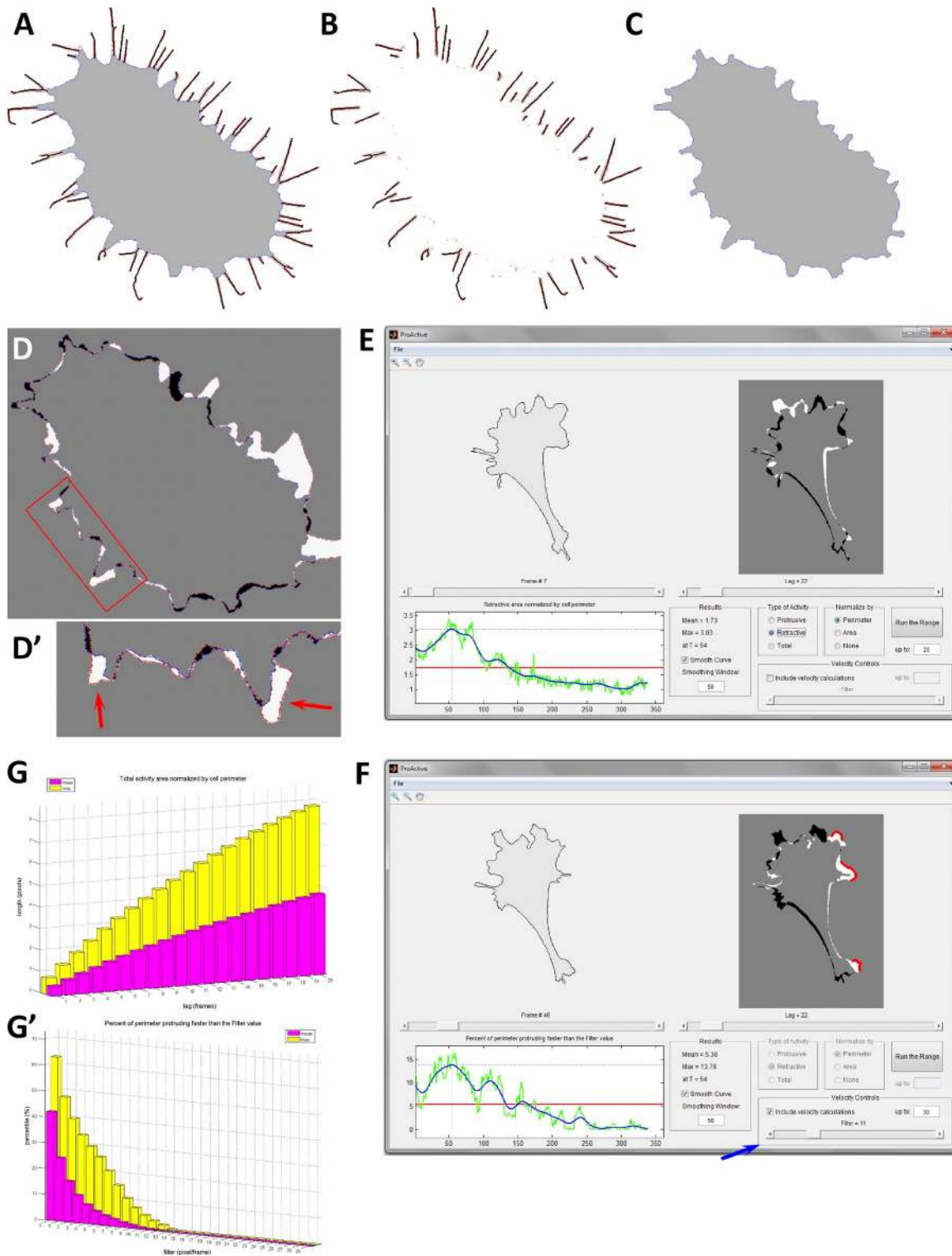
Figure 6.  **Detecting and quantifying dynamics of broad protrusion.** (A) Cell boundary. Filopodia skeletons are shown in black, and the cell body is shown in gray. (B and C) The cell is partitioned into filopodia (B) and cell body (C). (D and D') Changes in cell body shape can be tracked over time. The cell body at time *t* (blue) and *t* + 1 (red) with regions of protrusion in white and retraction in black. (D') Expanded view of the red box in D. Red arrows highlight broad, lamellipodial protrusions. (E) Screenshot of the ProActive module for detecting and quantifying broad protrusions. The cell body with filopodia removed is loaded in the left section above a scroll bar for selecting individual frames. The image on the right shows the change in cell body as in D with a scroll bar for selecting time lag. Protrusion, retraction, or both can be analyzed and normalized to cell perimeter or area (green curve). A smoothed curve through the data is shown in blue. (F) To correct for small cell body fluctuations, the velocity controls (blue arrow) allow users to set a minimum threshold for boundary velocity (indicated in red). (G and G') Selecting Run the Range graphs data for the mean and maximum activity for every time lag (G) or for every filter value (G') from 1 to the number typed in the up to box.

i.e., with a lag of 1. However, the time lag is an adjustable parameter, allowing users to compare cell body outlines at time frames that are farther apart in time, e.g., every 5, 10, and 20 frames. ProActive displays the mean and maximum protrusion activity as a function of lag. This provides insight into cell behavior: cells with more persistent protrusions show higher values of activity at larger lag values, even if at small lag values activity is indistinguishable. Setting the lag to the maximum (comparing the first and the last frame) provides a broad view of the overall shape change. Finally, if protrusive activity has a transient nature, e.g., changes caused by a drug treatment at a specific time, ProActive can identify the timing and level of peak activity for quantitative analysis of the cells' response to the stimulation.

ProActive also allows users to define the threshold for protrusions, allowing small cell boundary fluctuations to be filtered (Fig. 6 F illustrates exclusion of protrusions moving 8 pixels per frame or less). The remaining boundary movements (Fig. 6 F, marked in red) represent broad protrusions, such as lamellipodia. As with other parameters, this filter is fully adjustable for accurate detection using any cell type. Identified protrusions can then be followed over time and quantified as the fraction of the cell edge that protrudes.

Our approach is also applicable to quantitative analysis of cell polarization and motility. The broad protrusion profile makes areas of the cell that continually protrude (e.g., the leading edge) or retract easily recognizable and quantifiable, making our program widely applicable for characterizing both motile and nonmotile cells.

## Quantifying growth cone dynamics

CellGeo also includes the module ConeTrack developed for tracking neuronal growth cones. ConeTrack is a natural extension of FiloTrack and also relies on the BisectoGraph methodology (Fig. S5 B). The main user-defined parameters in ConeTrack that define growth cones are the critical radius of the growth cone $\Omega_{cr}$ and neck width $W_{cr} > \Omega_{cr}$. The critical radius $\Omega_{cr}$ is defined as the minimum allowed radius of the largest circle that fits into the growth cone. This parameter sets a minimum size for what structures are considered growth cones. The neck width $W_{cr}$ defines the "base" of the growth cone, that is, the end point of the narrow axon shaft between the growth cone and cell body. Using these two parameters, ConeTrack automatically identifies and tracks every cellular protrusion satisfying the definition of a growth cone.

## Validation and biological insights

**Filopodial and lamellipodial dynamics.** Filopodia are thought to sense chemotactic signals, whereas lamellipodia drive cell movement. Actin regulators control cell protrusion architecture, forming either branched or unbranched actin networks for lamellipodia or filopodia, respectively. Both protrusion types are important for morphogenesis, wound healing, and metastasis.

Many actin-associated proteins have overlapping or related functions, and it is unclear what roles they play in regulating protrusive behavior in vivo. To address this, we examined the roles of Dia and Ena, actin regulators promoting elongation of unbranched actin filaments (Goode and Eck, 2007; Bear and Gertler, 2009). Dia and Ena each regulate cell protrusions in vitro (Gertler et al., 1996; Bear et al., 2002; Peng et al., 2003; Gupton et al., 2007; Yang et al., 2007) and in vivo during normal development (Schirenbeck et al., 2005; Gates et al., 2007; Homem and Peifer, 2008, 2009) and during metastasis (Philippar et al., 2008; Sarmiento et al., 2008; Lizárraga et al., 2009). The precise roles of Dia and Ena in filopodial behavior in vivo and their relationship in this remain controversial. We also investigated the role of CP, which binds actin filament barbed ends to block elongation (Cooper and Sept, 2008). CP can be antagonized by Ena and Dia (Bear et al., 2002; Barzik et al., 2005; Schirenbeck et al., 2005; Gates et al., 2009; Hansen and Mullins, 2010), but the relative contributions of CP antagonism and barbed end polymerization by Dia and Ena to protrusion dynamics remains unclear. We thus explored how different combinations of these three actin regulators regulate the balance between filopodia and lamellipodia.

To do so, we used cultured *Drosophila* D16C3 cells, which naturally form both filopodia and lamellipodia with Dia and Ena present in both types of protrusions (Fig. 7, A and B). Dia and Ena are the single *Drosophila* Dia class formin or Ena/Vasodilator-stimulated phosphoprotein family members, making knockdown experiments straightforward. Protrusion dynamics were visualized using fluorescently labeled actin in time-lapse videos after overexpression or knockdown of Dia or Ena (Fig. 7, C–H′), and the resulting dynamics were analyzed using CellGeo (Fig. 8).

We first elevated levels of active protein by overexpressing either a constitutively active Dia mutant lacking the C-terminal Dia autoinhibitory domain (DAD; DiaΔDAD; Fig. 7, D and D′) or full-length Ena (Fig. 7, E and E′) to test the roles of Ena and Dia in driving filopodia or lamellipodia. Visual inspection revealed the expected increase of filopodia as compared with controls (Fig. 7 C), consistent with previous work (e.g., Bear et al., 2002; Schirenbeck et al., 2005; Gates et al., 2007; Yang et al., 2007). CellGeo allowed simple automated quantification of filopodia (Fig. 8 A), revealing an increase in both number and mean length (Videos 3 and 4). Interestingly, when we used the full range of tools in CellGeo, we found a second effect of Ena and Dia that was not obvious from visual inspection. Ena overexpression (Fig. 7 E′) or activating Dia (Fig. 7 D′) each significantly increased broad protrusions relative to controls (Fig. 7 C′ and Fig. 8 A). Thus, CellGeo revealed an effect on broad protrusiveness that was masked by the dramatic filopodia phenotypes (Videos 5 and 6). This highlights the versatility of CellGeo for analyzing both filopodia and lamellipodia in the same cell, making it unnecessary to limit analysis to cells with only a single protrusion type (e.g., Gupton et al., 2007).

Next, we used RNAi to knockdown Ena (Fig. 7, H and H′), Dia (Fig. 7, G and G′), or CP and examined effects on filopodia and lamellipodia. Although single knockdowns did not significantly affect broad protrusions (Fig. 7, F′, G′, and H′; and Fig. 8 B), Ena knockdown reduced filopodia number and length (Fig. 7 H and Fig. 8 B) relative to control cells (Fig. 7 F), whereas Dia knockdown had no effect (Fig. 8 B). Conversely,
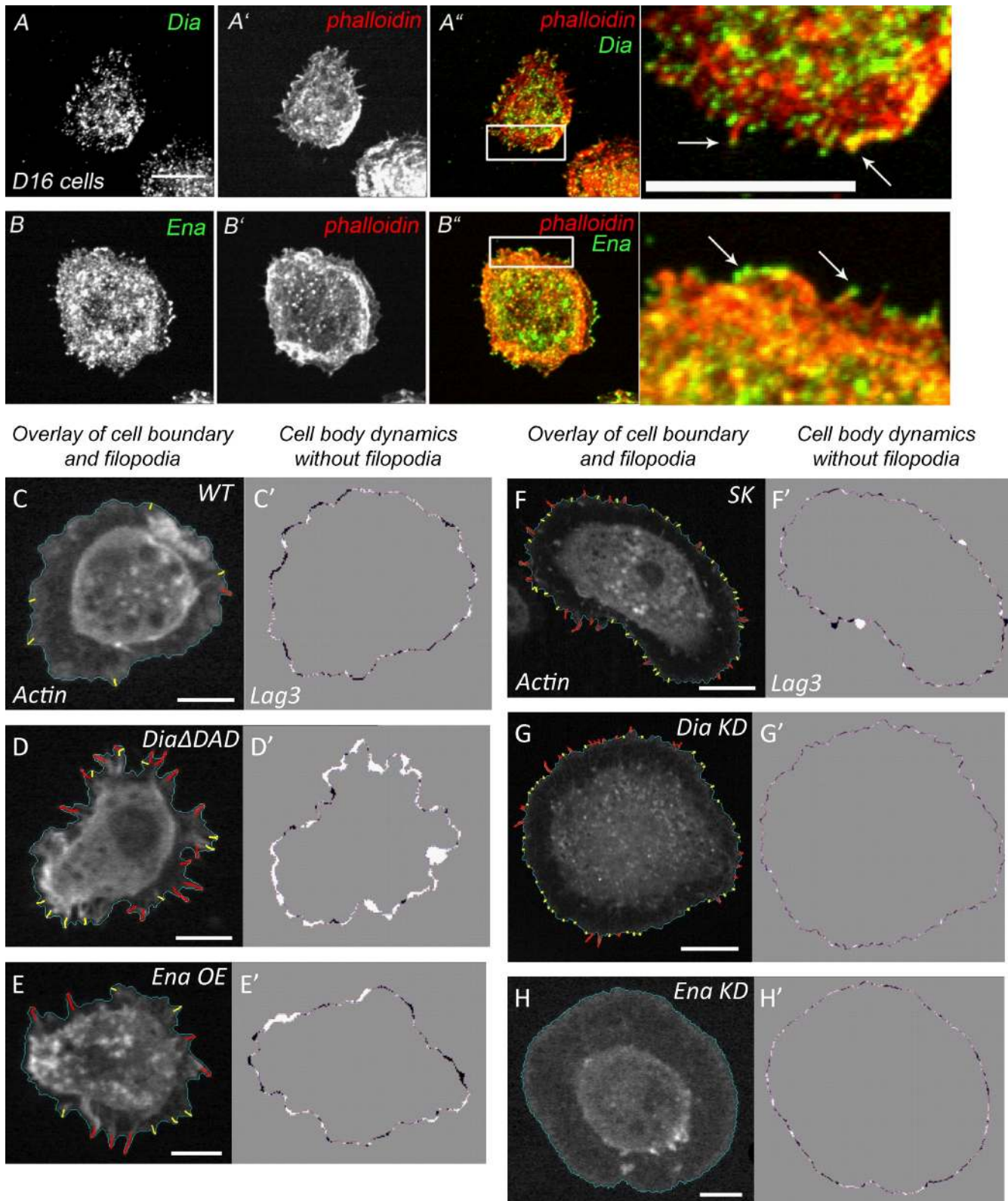
Figure 7. **CellGeo analysis of genetically manipulated D16C3 cells.** (A–A") *Drosophila* D16C3 cells stained for Dia (A) and phalloidin (A'). (A", inset) Dia at filopodia tips (left arrow) and cell cortex (right arrow). (B–B") D16C3 cells stained for Ena (B) and phalloidin (B'). (B", inset) Ena at filopodia tips (right arrow) and cell cortex (left arrow). (C–H) D16C3 cells expressing fluorescent actin and overlaid with the cell boundary (blue) and filopodia (red). Protrusions not meeting $L_{cr}$ are in yellow. (C'–H') Stills. Videos of broad protrusion dynamics (with filopodia removed) for cells in C–H in which every three frames are compared (lag 3). Cell bodies at time $t$ (red) or $t + 3$ (blue) with areas of protrusion in white and retraction in black. (C and C') Wild-type cell expressing actin alone. (D and D') DiaΔDAD expression. (E and E') Ena overexpression. (F and F') Control cell treated with SK RNAi (against BlueScript plasmid). (G and G') Dia knockdown. (H and H') Ena knockdown. KD, knockdown; OE, overexpression; WT, wild type. Bars: (C, D, E, H) 5 µm; (A, A" [inset], and F) 10 µm; (G) 15 µm.
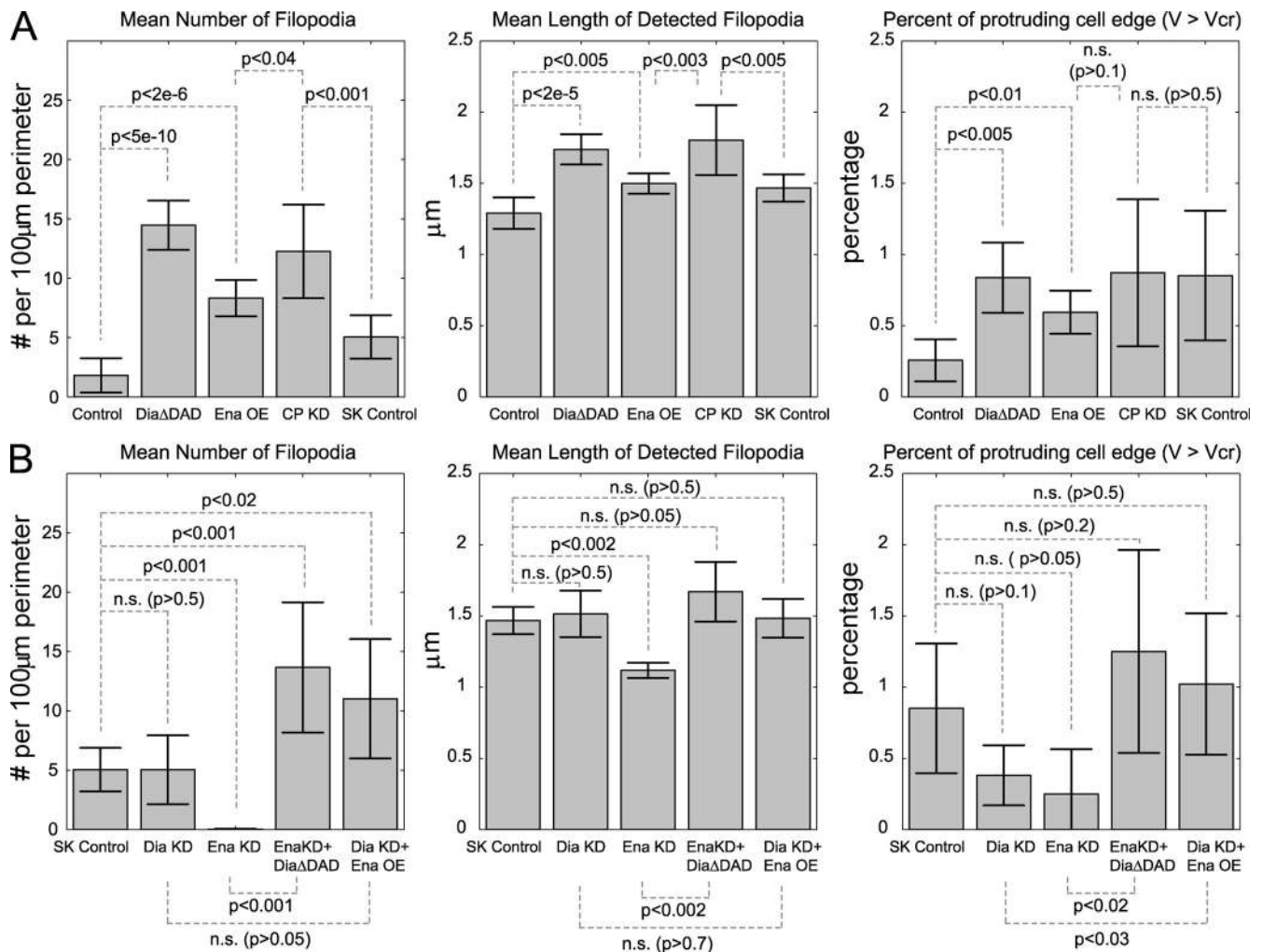
**Figure 8.** **Roles of Ena, Dia, and CP in regulating filopodia and broad protrusions.** (A and B) Quantification of filopodia number, length, and broad protrusion activity ($V_{cr}$ = 4 pixels/frame) of cells in overexpression and knockdown backgrounds. Numbers of cells used for analysis were actin $n = 16$, Dia$\Delta$DAD $n = 34$, Ena overexpression (OE) $n = 31$, SK knockdown (KD) $n = 21$, CP knockdown $n = 9$, Dia knockdown $n = 10$, Ena knockdown $n = 10$, Ena knockdown Dia$\Delta$DAD $n = 7$, and Dia knockdown Ena overexpression $n = 10$. Error bars show 95% confidence interval (mean ± two standard errors).

CP knockdown significantly increased filopodia number and length compared with SK (pBlueScript Sac1–Kpn1) controls (Fig. 8 A). Interestingly, CP knockdown also significantly increased filopodia number and length compared with Ena overexpression (Fig. 8 A), suggesting that even with high levels of Ena, some actin filament barbed ends remain protected by CP. Alternatively, CP knockdown could also affect Dia-based filopodia; however, Dia knockdown did not reduce filopodia number or length (Fig. 7 G and Fig. 8 B), suggesting that it is not essential for filopodia in these cells. Collectively, our data show that Ena is the primary unbranched actin elongator in D16C3 cells and suggest CP can block barbed end elongation even in the presence of high levels of Ena. In addition, Dia is not required for filopodia number or length in this cell type but may play an alternative role such as regulating cell adhesion (Homem and Peifer, 2008).

Next, we tested the relationship of Ena and Dia in controlling filopodia and broad protrusions by expressing activated Dia in Ena knockdown cells or overexpressing Ena in Dia knockdown cells. Dia$\Delta$DAD expression in Ena knockdown increased

filopodial number and length compared with Ena knockdown alone (Fig. 8 B). Ena overexpression significantly elevated filopodia number in Dia knockdown cells relative to SK controls (Fig. 8 B). Interestingly, although individual knockdowns of Ena, Dia, and CP did not significantly affect broad protrusions, overexpressing Ena significantly increased broad protrusions in Dia knockdown cells, and Dia$\Delta$DAD did so in Ena knockdown cells (Fig. 8 B). Together, these results suggest that Ena and Dia do not require each other to increase filopodia number and can act independently in formation of both filopodia and broad protrusions.

Collectively, our data provide new insights into how a single cell type utilizes these three actin regulators. In D16C3 cells, Ena plays the key role in promoting filopodia, with CP antagonizing this activity to balance protrusion number and length. Strikingly, CP knockdown is even more effective at elevating filopodial number and length than Ena overexpression, suggesting that blocking CP plays a quantitatively critical role in these parameters. Although Dia is not required for filopodia in these cells, an activated form can rescue filopodia number and length

and promote broad protrusions in cells with reduced Ena levels, suggesting that Dia can act independently if activated. We hypothesize that Ena and Dia are used differentially to create structurally similar protrusions with subtle but critical differences in dynamics and responsiveness to external cues. Further exploration of this hypothesis using CellGeo to analyze how Ena and Dia work together to shape protrusions is described in detail elsewhere (Bilancia et al., 2014). In summary, *CellGeo* can accurately detect and track filopodia and broad protrusions simultaneously in different genetic backgrounds with varying morphologies and quantify their dynamics for a precise, unbiased analysis.

### Neuronal growth cone dynamics

To demonstrate that CellGeo can be used for different protrusion geometries and different scales of motion and to further demonstrate its utility to generate new biological insights, we used it to assess the spatiotemporal dynamics of complex protrusions in neuronal growth cones. Though a large body of research suggests repulsive cues and collapse factors act through the GTPase RhoA (Sebök et al., 1999; Arakawa et al., 2003; Yuan et al., 2003; Mueller et al., 2005; Gallo, 2006; Loudon et al., 2006; McKerracher and Higuchi, 2006; Woo and Gomez, 2006; Birkenfeld et al., 2007), little is known about RhoA's role in regulating axon extension. Furthermore, growth cones rapidly move and change shape, making it difficult to quantitatively assess their dynamic behavior. To overcome this difficulty, we developed the module ConeTrack, which allows the immediate identification and tracking of growth cones. ConeTrack includes user adjustable parameters that can be optimized for each experiment based on morphological characteristics of the growth cones under study.

To study regulation of growth cone dynamics, we introduced the RhoA fluorescent activation reporter biosensor (Pertz et al., 2006) into catecholaminergic a–differentiated (CAD) neuroblastoma cells. Upon serum withdrawal, CAD cells differentiate and extend axons with motile growth cone–like structures that phenotypically mimic growth cones of primary neurons (Qi et al., 1997). Growth cone collapse and axon retraction can be induced by LPA stimulation. We used ConeTrack to analyze 27 time-lapse videos of CAD cells undergoing axon extension followed by collapse after LPA addition (Fig. 9 A). Because ConeTrack can simultaneously track multiple structurally distinct cellular features, for comparison, we also analyzed cell bodies (Fig. 9 B).

This provided several new insights into Rho regulation and growth cone dynamics. The pre-LPA time points revealed that active RhoA is already enriched at the edge of both advancing growth cones and cell bodies (Fig. 9 C). Strikingly, although stimulating the cells with LPA caused the expected global increase in RhoA activation, it did not change the shape of the activity distribution profiles (Fig. 9 C), with a similar degree of enrichment at the cortex relative to the interior. In growth cones, peak RhoA activation occurred earlier than in cell bodies (Fig. 9 D) and on average preceded initiation of growth cone collapse (Fig. 9, A and E). After peak RhoA activity, growth cone RhoA activity levels rapidly dropped (coincident with collapse), whereas cell body RhoA activity was maintained at an elevated level (Fig. 9 D). These results provide new spatiotemporal insights into growth cone collapse, suggesting elevated RhoA levels in growth cones are required to initiate but not to sustain or complete collapse. Interestingly, our analysis also revealed a novel, unexpected aspect of growth cone behavior. We found that the time delay between LPA treatment and growth cone collapse is inversely proportional to the growth cone's size (Fig. 9 F). Although it is too early to speculate on the exact mechanisms underlying this phenomenon, our analysis provides new insights into axon repulsion and once again demonstrates the power of CellGeo for extracting quantitative information on complex morphodynamic behavior not readily obtainable by visual inspection.

## Discussion

CellGeo provides a highly flexible computational platform for defining, measuring, and dynamically tracking cell protrusions and other changes in morphology. Our tree graph representation of the cell boundary overcomes the computationally challenging problem of precisely defining protrusions and provides efficient methods for quantifying key characteristic features of protrusions and cell body dynamics simultaneously.

We demonstrated the power and versatility of CellGeo by using it to analyze the roles of the actin regulators Ena, Dia, and CP in cell protrusion dynamics in cultured *Drosophila* cells, revealing their distinct roles in filopodial dynamics. We also applied the tool to study growth cone dynamics in CAD neuroblastoma cells and the distribution of RhoA GTPase activity in both protruding and retracting growth cones, revealing new insights into growth cone regulation.

In its current form, CellGeo is built for applications with 2D cell images. However, the BisectoGraph methodology is not limited to 2D. There are two ways our approach could naturally be extended to 3D analysis. The first method involves using a z stack to render the cell outline as a 3D surface (or a polyhedron) and then building a 3D tree graph inside the resulting 3D shape. The second method is to extract 2D features in each z-stack plane and "stitch" the extracted 2D features together to form a 3D representation. We are currently applying the second approach to analyze the organization and dynamics of fungal biofilms (*Candida albicans*) in 3D. Imaging in 3D, particularly in vivo, will present challenges as a result of the potential decrease in signal to noise ratio. This only becomes an issue if it becomes too low to allow extraction of the cell boundary.

Although we focused on protrusions, the computational methods in CellGeo are broadly applicable for studying cell shape dynamics. For example, we are currently using CellGeo to morphologically analyze dendritic spines in neurons, allowing us to accurately measure and differentiate between the spine qualities (thin, stubby, mushroom, and branched) observed during neuronal development. Moving further afield, the method can be applied to quantify growth and structural development of multicellular formations. For example, we are currently using CellGeo to study how the organization and dynamics of fungal biofilms influence leukocyte infiltration. Thus, our computational method will prove useful to a wide array of scientists
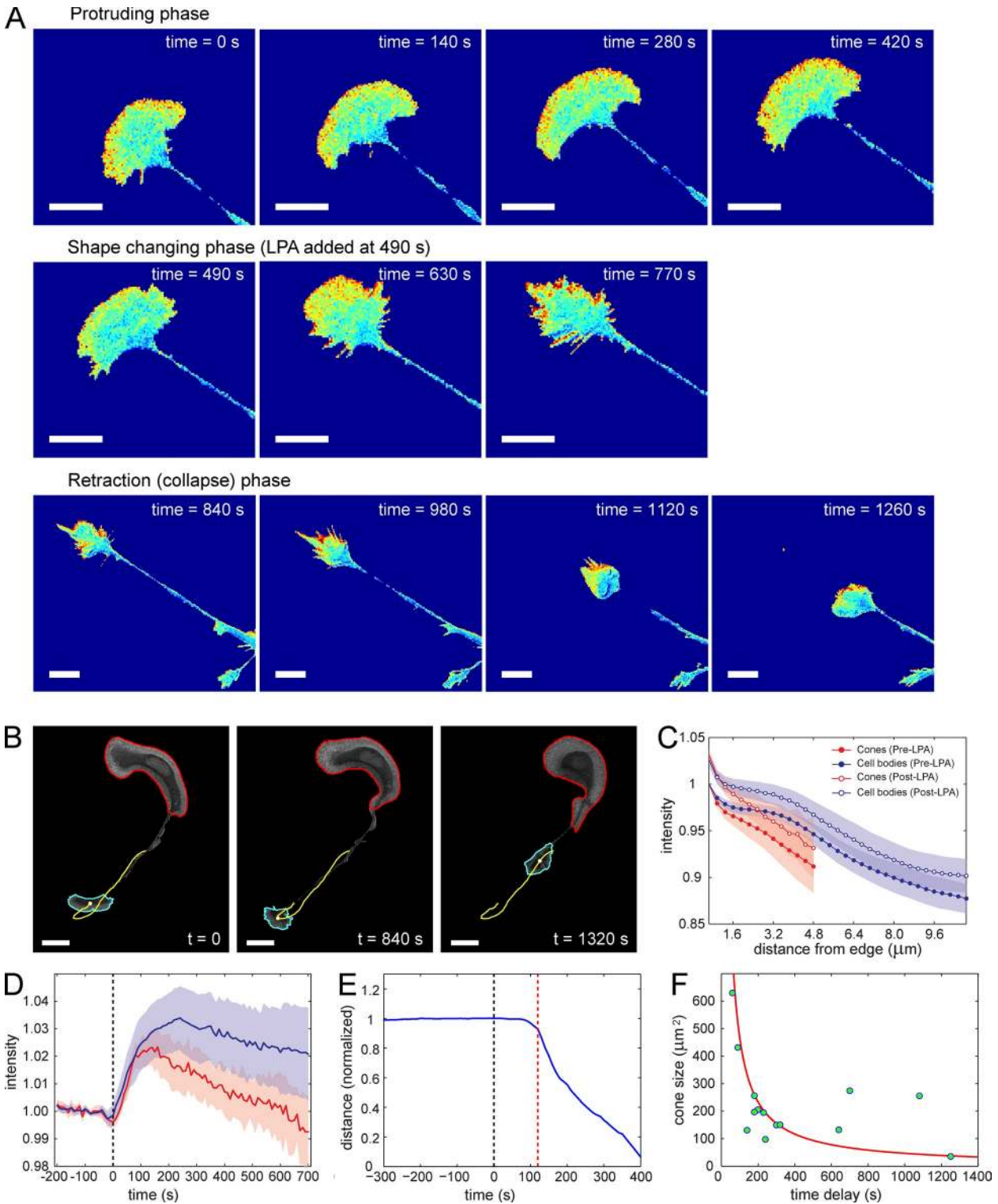
Figure 9. **Growth cone dynamics and RhoA regulation in CAD neuroblastoma cells.** (A) Illustration of growth cone dynamics and RhoA biosensor activity in CAD cells as a timeline showing three distinct phases: protruding (top row), reshaping (middle row), and collapse (bottom row). The last two occur after LPA treatment. Bars, 10 µm. (B) CAD cell with the growth cone (cyan) and cell body (red) identified by ConeTrack at three time points. Yellow curves show the trajectory of growth cone's centroid. Bars, 20 µm. (C) Distribution of RhoA biosensor activity in growth cones (red) and cell bodies (blue) before (filled circles) and after (empty circles) LPA treatment. (D) Mean intensity of RhoA biosensor activity at cell edge in growth cones (red) or cell bodies (blue) as a function of time. Black dashed line shows the time point when LPA was added. (C and D) Shaded areas show 95% confidence intervals ($n = 19$ growth cones; $n = 15$ cell bodies). (E) Distance from current position of growth cone's centroid to its terminal position, normalized by distance at time of LPA treatment (black dashed line). The onset of growth cone retraction (red dashed line) is delayed with respect to time of LPA treatment. (F) Correlation between time delay in growth cone retraction and growth cone size immediately preceding LPA treatment ($n = 14$). Red curve shows a fit to the data using the function y = constant/x.

studying different biological systems that require automated statistical quantification of geometric and dynamic properties of the edge. Our user-friendly interface CellGeo allows researchers to both study geometric aspects of their cell type in detail and collect statistical results in an automated and accurate manner.

# Materials and methods

### Cell culture and immunohistochemistry

*Drosophila* D16C3 cells were cultured in Schneider's media supplemented with 10% fetal bovine serum, 1% penicillin–streptomycin, and 10 µg/ml recombinant human insulin (Gibco/Life Technologies). For overexpression experiments, FuGENE HD (Promega) was used to transfect cells with pIZ GFP-actin or pIZ monomeric Cherry (mCh)–actin for controls, pIZ GFP-actin and pIZ mCh-Ena for Ena overexpression, or pIZ mCh-actin and pIZ GFP-DiaΔDAD for activated Dia expression (mCh constructs were a gift from the Rogers laboratory, University of North Carolina–Chapel Hill, Chapel Hill, NC). Cells were plated on poly-D-lysine–coated glass-bottom dishes (MatTek Corporation) and imaged 48–72 h later. For RNAi, D16C3 cells were plated in 12-well dishes to 75% confluency and treated with 10 µg of double-stranded RNA in fresh growth media on days 1, 4, and 8. On day 12, cells were transfected and plated as stated in this paragraph.

For immunohistochemistry, *Drosophila* D16C3 cells were plated on glass coverslips and fixed in 10% paraformaldehyde in PBS (EM Sciences) for 10 min. Cells were permeabilized with 0.1% Triton X-100, blocked with 5% normal goat serum, and stained for Ena (1:500; Developmental Studies Hybridoma Bank) or Dia (1:5,000; gift from S. Wasserman, University of California, San Diego, San Diego, CA). We used Alexa Fluor 488–conjugated goat anti–mouse or anti–rabbit secondary antibodies (1:500; Molecular Probes), and actin was labeled with TRITC-phalloidin (1:1,000; Sigma-Aldrich). Slides were mounted in Aqua-Poly/Mount (Polysciences, Inc.).

CAD cells were cultured in DMEM/F12 medium (Gibco) supplemented with 8% fetal calf serum, 1% L-glutamine, and 1% penicillin–streptomycin. They were imaged in Ham's F-12K medium without phenol red (SAFC Biosciences) supplemented with 15 mM Hepes, 1% L-glutamine, and 1% penicillin–streptomycin. To induce differentiation, cells were plated on coverslips coated with 18 µg/ml laminin (Sigma-Aldrich). After 90 min, normal culture medium was exchanged for imaging medium. Cells were allowed to differentiate for an additional 90–120 min before imaging. CAD cells were transfected 12–24 h before imaging with the RhoA biosensor using FuGENE 6 (Roche) according to manufacturer's instructions. 3 µM LPA (Sigma-Aldrich) was used for LPA stimulation experiments.

### Microscopy

Imaging of *Drosophila* D16C3 cells was performed with a 100×, 1.4 NA oil objective (Nikon) on an inverted spinning-disc confocal imaging system (Wallac UltraVIEW; PerkinElmer). Live imaging of GFP- and mCh-tagged constructs was performed at room temperature in Schneider's media. Images were collected every 2 s for a minimum of 2 min using MetaMorph software (Molecular Devices) and a camera (ORCA-ER; Hamamatsu Photonics). Brightness and contrast were adjusted using ImageJ (National Institutes of Health). At least three replicates were analyzed for controls and experimental conditions for both live and fixed imaging. Quantification of live-imaging videos was performed on 7–34 cells.

CAD cell imaging was performed on a motorized inverted microscope (IX81; Olympus) equipped with Z-drift compensator focus drift compensator and total internal reflection fluorescence microscope illuminator, a cooled digital 12-bit charge-coupled device camera (CoolSNAP; Roper Scientific), a 100-W Mercury arc lamp, and MetaMorph imaging software. Images were acquired using a 40× U Plan Fluor N, 1.3 NA objective. A multipass dichroic mirror (89006bs; Chroma Technology Corp.) was used with the following band pass filters: CFP (436/20- and 480/40-nm excitation filters) and Förster resonance energy transfer (436/20- and 540/30-nm excitation filters). Coverslips were mounted in a live-cell chamber (Attofluor; Invitrogen) and placed on a microscope stage with a heated stage adaptor (Warner) that maintained samples at 37°C. Förster resonance energy transfer/CFP ratio images were calculated after shading correction, background subtraction, binary masking, and image registration using MetaMorph and MATLAB software (MathWorks, Inc.) as previously described (Pertz et al., 2006). Photobleach correction was performed with custom MATLAB software that fits the fluorescence decay of the ratio

intensity over time to a double exponential function and then applies that function back to the original images (Hodgson et al., 2006). Time points immediately after LPA stimulation were excluded from fitting.

### Boundary representation

A boundary can be represented as a continuous analytical function $B(x(s), y(s))$ or a discrete set of connected edges in the form of lines, circular arcs, B-splines, conic sections, or other geometric representations. In all cases, algorithms exist to construct a medial axis representation of the boundary (Fig. 1, C–F). The simplest and most common representation of an object, such as a cell, in a binary image is a closed polygonal chain with linear segments connecting the centers of neighboring pixels on the boundary of the object (Fig. S2, A–C). Such a polygonal chain can be constructed using the standard Moore-Neighbor tracing algorithm. In addition to being computationally efficient and simple, this method preserves the discrete nature of the input data and does not involve any preprocessing. However, in general, there are two special cases associated with this representation that need to be dealt with: self-crossings and degeneracies.

**Self-crossing.** Self-crossing refers to the situation in which polygonal chain representation of the boundary contains intersections or overlaps (Fig. S2, A, D, and E). A simple closed polygonal chain does not contain any self-crossings. The MAT of a simple closed polygonal chain is a tree graph emanating from a single root with each branch of the graph eventually ending at a unique boundary point (Fig. 1, C–F; and Fig. 3 D). We refer to a sequence of graph edges from the root to the boundary as a path. In contrast, self-crossings create additional features in the resulting MAT. For example, a single path might go through several boundary points, or some graph edges might overlap with boundary edges. There are two options for dealing with self-crossings. One is to keep track of all self-crossings and the special features they generate in the MAT at each stage of cell shape analysis. The second is to regularize the boundary at the beginning of analysis and only deal with MATs in their simplest form. We follow the second option. To regularize the boundary, we first eliminate (set the intensity value to 0) all boundary points with an internal angle (i.e., the angle inside a polygon between two adjacent sides) equal to 0 (Fig. S2 D) and retrace the boundary. This step needs to be repeated until no such points are present. Alternatively, one can modify the boundary-tracing algorithm, so that unwanted boundary points get eliminated as the tracing progresses. Removing boundary points with internal angles of 0 effectively removes all boundary extensions of 0 width (i.e., all cell protrusions of 1-pixel width). All other crossings (such as in Fig. S2 E) can be regularized by 1-pixel dilation of the corresponding boundary pixels (i.e., setting the intensity values of their four nearest neighbors to 1). Our solution to this problem, which involves adding or removing a single pixel, only affects the data locally and on a scale of no more than 1 pixel.

**Degeneracy.** Consider for a moment a regular $N$-sided polygon as a boundary. The MAT of this boundary consists of a single vertex at the center and $N$ edges connecting it with the boundary points (Fig. S3 A). The single vertex is degenerate in the sense that a small random perturbation to the polygon produces a MAT with $N - 2$ vertices (located near the geometric center), each with exactly three edges (Fig. S3, B and C). Similarly, a simple closed polygonal chain on a regular square grid will likely generate degenerate vertices with more than three graph edges. Although, technically, this is not a problem: because the MAT is still a tree and the cell shape analysis can be performed for the degenerate cases, nondegenerate MATs have well-characterized topological structures and simple geometric rules for how edges meet at vertices, which we take advantage of in our graph-building algorithm (see Tree graph representation). Thus, we prefer to deal with nondegenerate MATs after applying random perturbations to boundary coordinates on a scale of a fraction of the pixel size.

### Tree graph representation

The tree graph generated by the MAT provides unique paths located inside the cell from the root to all convex boundary points but not to the concave points (Fig. S2 F). To construct a complete boundary profile with a distance measure from the root to all boundary points, the graph needs to be extended to include edges connecting concave points to the graph. This can be done by considering the Voronoi diagram inside the boundary representation. The Voronoi diagram inside a simple closed polygonal chain is a union of the medial axis with all pairs of rays originating from concave boundary points at angles perpendicular to the neighboring boundary edges and ending on the graph generated by the MAT (Fig. S4). The resulting nondegenerate graph still has all internal vertices of order 3. However, strictly speaking, such a graph is not a tree because there are two alternative paths connecting the root with each concave boundary point.

If the goal is to identify and track cell protrusions, it is sufficient to use the tree graph generated by the MAT. However, as we show in the previous paragraph, the Voronoi graph is more useful for identifying the cell body independent of filopodia. Moreover, our graph construction algorithm relies on the geometric structure of the whole Voronoi graph, so that there is no reason to limit the graph to the subset of vertices defined by the MAT.

Each edge of the medial axis graph bisects the space between two boundary components, which are either lines ($\lambda$, boundary edges) or points ($\rho$, boundary vertices). Thus, the edges of the MAT consist of three types of curves: (1) $\mu_{\lambda\lambda}$, which bisect space between two lines, (2) $\mu_{\lambda\rho}$, which bisect space between a line and a point, and (3) $\mu_{\rho\rho}$, which bisect space between two points. The Voronoi graph also includes edges $\mu_\nu$ that connect concave boundary point with the MAT. The curves $\mu_{\lambda\lambda}$, $\mu_{\rho\rho}$, and $\mu_\nu$ are lines, whereas $\mu_{\lambda\rho}$ are parabolas.

When two edges of the Voronoi graph meet/collide at a vertex (an event denoted as $\otimes$), the third edge emerges (an event denoted as $\Rightarrow$) according to the following rules: $\mu_{\lambda\lambda} \otimes \mu_{\lambda\lambda} \Rightarrow \mu_{\lambda\lambda}$ (1), $\mu_{\lambda\lambda} \otimes \mu_\nu \Rightarrow \mu_{\lambda\rho}$ (2), $\mu_{\lambda\lambda} \otimes \mu_{\lambda\rho} \Rightarrow \mu_{\lambda\rho}$ (3), $\mu_{\lambda\rho} \otimes \mu_\nu \Rightarrow \mu_{\lambda\lambda}$ or $\mu_{\rho\rho}$ (4), $\mu_{\lambda\rho} \otimes \mu_{\lambda\rho} \Rightarrow \mu_{\lambda\lambda}$ or $\mu_{\rho\rho}$ (5), $\mu_{\lambda\rho} \otimes \mu_{\rho\rho} \Rightarrow \mu_{\lambda\rho}$ (6), $\mu_{\rho\rho} \otimes \mu_\nu \Rightarrow \mu_{\lambda\rho}$ (7), and $\mu_{\rho\rho} \otimes \mu_{\rho\rho} \Rightarrow \mu_{\rho\rho}$ (8). The exact orientation of the emerging graph edge is defined by the position of the boundary components to be bisected, which is determined at the collision event, because each colliding edge donates one of two boundary components associated with it to the emerging edge. Thus, all vertices of the Voronoi diagram can be found in an iterative process starting from the boundary and following the collision rules 1–8 until the graph eventually converges at the root. Fig. S4 (A–F) illustrates this iterative algorithm and the rules 1–7.

If the boundary consists of $N$ points, $k$ of which are concave and $(N - k) \geq 3$ are convex, the total number of vertices in the Voronoi graph excluding the points on the boundary is $N + k - 2$. If the boundary points are included, the number of vertices becomes $2N + k - 2$. When only the MAT is of interest, $k$ vertices on the boundary and $2k$ corresponding vertices inside the boundary can be ignored (Fig. S4, D and G) so that the remaining MAT consists of $N - k - 2$ and $2N - 2k - 2$ vertices, excluding and including boundary points, respectively. Correspondingly, the number of edges is $2N + 2k - 3$ in the Voronoi graph and $2N - 2k - 3$ in the MAT. Importantly, no matter whether we consider the Voronoi or medial axis graph, the tree graph representation requires the storage of less than $2N$ points. To be more specific, it is between $N - 2$ and $2N - 5$ for the Voronoi graph and between $1$ and $N - 2$ for the MAT, depending on the number of concave points, $0 \leq k \leq (N - 3)$. Fig. S4 (G–I) illustrates these numbers with $N = 7$ and $k = 4$, so that the MAT (Fig. S4 H) consists of four vertices ($2N - 2k - 2$)—three on the boundary ($N - k$) and one inside ($N - k - 2$)—and three edges ($2N - 2k - 3$). The corresponding Voronoi graph (Fig. S4 I) consists of 16 vertices ($2N + k - 2$)—seven on the boundary ($N$) and nine inside ($N + k - 2$)—and 19 edges ($2N + 2k - 3$).

## Boundary profile

The tree graph representation of the cell boundary (MAT) has several particularly useful features for shape analysis. First, the graph is entirely contained within the interior of the cell, and each boundary point is connected to the tree root by a medial path. This feature provides a mechanism to measure distances from an arbitrarily irregular boundary to the cell center. Importantly, each local maximum in the plot of such distances, $P(n)$, as a function of the boundary point labels ($n = 1, 2 \ldots N$) corresponds to the tip of an outward extension on the boundary (i.e., cell protrusion). Protrusions might have very different geometries, but the key step in quantifying their geometries is the ability to accurately and robustly identify a single reference point, the tip.

We will be distinguishing two variations of the boundary profiles, $P(n)$ and $P'(n)$. The first, $P(n)$, only considers distances measured to the convex boundary points along the edges of the MAT graph, whereas $P'(n)$ includes distances measured from both convex and concave points along the edges of the Voronoi graph. Unlike convex points, concave boundary points are connected with the root by two different paths so that two values of the distance are associated with each concave point. Thus, to deal with a single-valued boundary profile, we will use the mean of the two distances (alternatively, one can use the smallest of two values). Obviously, protrusion tips should not be sought among concave boundary points. $P(n)$ is sufficient for that purpose, but $P'(n)$ is a profile of the whole boundary with no points taken out of consideration. This becomes useful when, for example, one needs to reconstruct the boundary from a truncated graph (see Quantifying the shape and dynamics of broad protrusions).

Although, the length of the parabolic segments can be found exactly, we can simplify and speed up shape profiling by approximating the parabolic edges by lines. Formally, this means that we consider exact coordinates of all graph vertices (as found by a graph-building algorithm) but measure distances along the straight lines between the vertices on the corresponding graph paths. This approximation does not alternate the topology of the graph. The shape features that might be affected by this approximation are on a scale similar to that of the inaccuracies in boundary detection and of no interest to us.

**Sensitivity to noise.** One of the major disadvantages of the MAT that limits its application is its sensitivity to noise. Very small fluctuations of the boundary might significantly alter the form of the graph. Fortunately, such sensitivity does not affect the important properties of the boundary profile. Indeed, a graph perturbed by fluctuations still produces a boundary profile with local maxima corresponding to the tips of protrusions. Because we do not directly compare graphs, but only the extracted profiles, the sensitivity to noise is not an issue (Fig. 2). Again, we note that protrusions with a length scale of random boundary fluctuations are not of interest.

## Filopodia identification

As described in the first section of the Results (see also Fig. 4), a very convenient feature of the medial axis is that by construction each point of the graph is the center of a circle that is tangent to two or more boundary edges, which serves as a measure of the protrusion width. However, there are two easily resolvable complications associated with this approach.

**Uniqueness.** As long as $R_{cr} < R_{max}$, then Eq. 1 in the Results has a solution, but it is not necessarily unique. Indeed, a filopodium might be slightly wider than the critical width at several places along its skeleton. The simplest solution to the nonuniqueness problem is to use for $L_{pr}$ the first intersection of $R(L)$ and $R_{cr}$. However, in this case, if the typical scale for the filopodia width is too close to the critical value $R_{cr}$, filopodia might be cut off at length shorter than would be performed by visual inspection. Thus, one needs either to choose a bigger value for the parameter $R_{cr}$ or to use $L_{pr}$, which corresponds to the last intersection of $R(L)$ and $R_{cr}$. In the second case, it is useful to introduce a tolerance, $\varepsilon > 0$, and choose the largest of $L_{pr}$'s, satisfying Eq. 1 on the interval from 0 to the point where $R(L)$ intersects with $R_{cr} + \varepsilon$ for the first time. This ensures proper identification of filopodia for relatively large cell extensions (such as neuron growth cones or spines) that are connected with the main cell body by a narrow link.

**Branching.** As shown in Fig. 4 C, filopodia skeletons may overlap near the base. Thus, if the mean length of filopodia is the quantity of interest, the contribution from some fragments of cell protrusions will be counted twice or more. Once again, this might be an indicator of a poorly chosen critical radius $R_{cr}$ (compare Fig. 4, B and B' with C and C'). However, if the adjustment of parameters is not an option, a simple way to avoid overcounting is to use full-length $L_{pr}$ only for the longest of the partially overlapping skeletons. For each of the remaining skeletons, the base needs to be redefined as the point where the overlap occurs, i.e., at the branching point. Because of the tree structure of the MAT, this procedure is well defined and straightforward even for the case of consecutively branching filopodia.

## Filopodia tracking

To track filopodia, one needs to specify a distance measure and criteria that have to be satisfied to associate a filopodium $p$ at time $t$ with a filopodium $q$ at time $t + 1$. Let $\vec{r}_i^{\,p} = \left( x_i^p, y_i^p \right)$ and $\vec{r}_j^{\,q} = \left( x_j^q, y_j^q \right)$ be the skeleton coordinates for a pair of filopodia ($p$, $q$), in which $i = 1, 2 \ldots N_p$ and $j = 1, 2 \ldots N_q$, and without loss of generality, let the number of skeleton points be $N_p \leq N_q$. Then, we define the distance between $p$ and $q$ as

$$D_{p,q} = \left\langle \min_j \left\| \vec{r}_i^{\,p} - \vec{r}_j^{\,q} \right\| \right\rangle_i ,$$

in which $\langle \ \rangle_i$ denotes the mean over index $i$, and the norm $\| \vec{r} \|$ is the Euclidean distance between two points. Alternatively, instead of the simple mean value, one can use the maximum or the minimum value:

$$D_{p,q} = \max_i \left( \min_j \left\| \vec{r}_i^{\,p} - \vec{r}_j^{\,q} \right\| \right) \text{ or }$$

$$D_{p,q} = \min_i \left( \min_j \left\| \vec{r}_i^{\,p} - \vec{r}_j^{\,q} \right\| \right) .$$

Thus, the matrix $D(p,q)$ tells us how far each filopodium at time $t + 1$ is positioned with respect to each filopodium at time $t$.

Introducing a critical distance, $D_{cr}$, for each filopodium $q_k(t + 1)$, we find filopodia $p_m(t)$ that satisfy the condition

$$D(p_m, q_k) < D_{cr}. \qquad (2)$$

If no such $p_m$ is found, filopodium $q_k$ is considered to be a newly formed at time $t + 1$. For the other $q_k$'s, we find a pair $(p_M, q_k)$ with the smallest distance

$$D(p_M, q_K) = \min_{m,k} D(p_m, q_k),$$

remove the pair from further consideration, and recheck the aforementioned condition for the remaining filopodia. This step is repeated until all pairs are found. The full procedure is repeated consecutively for each time frame so that each filopodium is tracked from the time it appears (i.e., was paired for the first time with a filopodium at the next time frame) to the time it disappeared (i.e., had no pair among filopodia at the following frame). Filopodia that have never been paired are considered to have a lifetime of one frame.

**Gap filling.** Often there is a need to correct for temporary disappearance (blinking) of filopodia caused by detection issues. The problem can be avoided by filling the gap in the following way. Once all pairs of filopodia $p_m(t)$ and $q_k(t + 1)$ from time points $t$ and $t + 1$ are found, unpaired filopodia at time $t + 1$ are compared with filopodia at time $t − 1$ on the bases of the condition (Eq. 2). This will identify all filopodia that blinked for an interval of one time step. If there are still unpaired filopodia left, they are compared with filopodia at time $t − 2$. The procedure is continued until all gaps up to a desired duration $G_{cr}$ are filled. Only after that, filopodia $q_k(t + 1)$ that are still unpaired are considered nascent structures, and the algorithm proceeds to the next time frame. The value of the maximum time gap $G_{cr}$ should be chosen based on biological considerations. If a filopodium retracts and then a new one is formed in about the same place, it will be tracked separately only if $G_{cr}$ is shorter than the time of such reformation. Thus, in most cases, taking $G_{cr}$ to be one or two time frames should be sufficient to eliminate the blinking effect without overestimating filopodia lifetimes. In any case, a pair of parameters $(D_{cr}, G_{cr})$ precisely specifies the rules by which tracking is performed.

### Statistical analysis
For data analysis in Fig. 8 and Fig. 9, we used mean values and two standard errors (as 95% confidence interval indicated by error bars) of measurement for individual cells. In Fig. 8, p-values were found using two-sample *t* test (built-in MATLAB function ttest2). The measurements of filopodia number and percentages of protruding cell edge for individual cells were averaged over the time frames of the time-lapse videos. The measurements of filopodia length for individual cells were averaged over all tracked filopodia during the time-lapse videos.

### Online supplemental material
Fig. S1 shows the MovThresh module for detecting cell boundaries. Fig. S2 shows examples of boundary representations and self-crossing events. Fig. S3 shows examples of degenerate and nondegenerate MATs. Fig. S4 illustrates the collision algorithm and counting of vertices and edges for MATs and Voronoi graphs. Fig. S5 shows the BisectoGraph and ConeTrack modules. Video 1 illustrates a MAT interpretation. Video 2 shows an example of a D16C3 cell with a large number of filopodia identified by Cell-Geo. Video 3 shows FiloTrack analysis of a control D16C3 cell. Video 4 shows FiloTrack analysis of a D16C3 cell expressing activated Dia, revealing an increase in filopodia number and length compared with control cells. Video 5 shows ProActive analysis of the same control D16C3 cell shown in Video 3. Video 6 shows ProActive analysis of the same D16C3 cell expressing activated Dia shown in Video 4, revealing an increase in broad protrusions compared with control cells. A ZIP file is also provided that includes the CellGeo package, which includes five folders corresponding to the five modules: MovThresh, BisectoGraph, FiloTrack, ConeTrack, and ProActive. Each folder contains MATLAB codes, data examples, and a text file with instructions on how to use the module (input format, output format, and processing steps). Online supplemental material is available at http://www.jcb.org/cgi/content/full/jcb.201306067/DC1.

## References

Abeysinghe, S., T. Ju, M.L. Baker, and W. Chiu. 2008. Shape modeling and matching in identifying 3D protein structures. *Comput. Aided Des.* 40:708–720. http://dx.doi.org/10.1016/j.cad.2008.01.013

Aichholzer, O., W. Aigner, F. Aurenhammer, T. Hackl, B. Jüttler, and M. Rabl. 2009. Medial axis computation for planar free-form shapes. *Comput. Aided Des.* 41:339–349. http://dx.doi.org/10.1016/j.cad.2008.08.008

Arakawa, Y., H. Bito, T. Furuyashiki, T. Tsuji, S. Takemoto-Kimura, K. Kimura, K. Nozaki, N. Hashimoto, and S. Narumiya. 2003. Control of axon elongation via an SDF-1α/Rho/mDia pathway in cultured cerebellar granule neurons. *J. Cell Biol.* 161:381–391. http://dx.doi.org/10.1083/jcb.200210149

Aurenhammer, F. 1991. Voronoi Diagrams - a Survey of a Fundamental Geometric Data Structure. *ACM Comput. Surv.* 23:345–405. http://dx.doi.org/10.1145/116873.116880

Barzik, M., T.I. Kotova, H.N. Higgs, L. Hazelwood, D. Hanein, F.B. Gertler, and D.A. Schafer. 2005. Ena/VASP proteins enhance actin polymerization in the presence of barbed end capping proteins. *J. Biol. Chem.* 280:28653–28662. http://dx.doi.org/10.1074/jbc.M503957200

Bear, J.E., and F.B. Gertler. 2009. Ena/VASP: towards resolving a pointed controversy at the barbed end. *J. Cell Sci.* 122:1947–1953. http://dx.doi.org/10.1242/jcs.038125

Bear, J.E., T.M. Svitkina, M. Krause, D.A. Schafer, J.J. Loureiro, G.A. Strasser, I.V. Maly, O.Y. Chaga, J.A. Cooper, G.G. Borisy, and F.B. Gertler. 2002. Antagonism between Ena/VASP proteins and actin filament capping regulates fibroblast motility. *Cell.* 109:509–521. http://dx.doi.org/10.1016/S0092-8674(02)00731-6

Bilancia, C.G., J.D. Winkelman, D. Tsygankov, S.H. Nowotarski, J.A. Sees, K. Comber, I. Evans, V. Lakhani, W. Wood, T.C. Elston, et al. 2014. Enabled negatively regulates Diaphanous-driven actin dynamics in vitro and in vivo. *Dev. Cell.* In press.

Birkenfeld, J., P. Nalbant, B.P. Bohl, O. Pertz, K.M. Hahn, and G.M. Bokoch. 2007. GEF-H1 modulates localized RhoA activation during cytokinesis under the control of mitotic kinases. *Dev. Cell.* 12:699–712. http://dx.doi.org/10.1016/j.devcel.2007.03.014

Blum, H. 1967. A transformation for extracting new descriptors of shape. *In* Models for the Perception of Speech and Visual Form: Proceedings of a Symposium. W. Wathen-Dunn, editor. MIT Press, Cambridge, MA. 362–380.

Chin, F., J. Snoeyink, and C.A. Wang. 1999. Finding the medial axis of a simple polygon in linear time. *Discrete Comput. Geom.* 21:405–420. http://dx.doi.org/10.1007/PL00009429

Cooper, J.A., and D. Sept. 2008. New insights into mechanism and regulation of actin capping protein. *Int. Rev. Cell Mol. Biol.* 267:183–206. http://dx.doi.org/10.1016/S1937-6448(08)00604-7

Costantino, S., C.B. Kent, A.G. Godin, T.E. Kennedy, P.W. Wiseman, and A.E. Fournier. 2008. Semi-automated quantification of filopodial dynamics. *J. Neurosci. Methods.* 171:165–173. http://dx.doi.org/10.1016/j.jneumeth.2008.02.009

Etienne-Manneville, S., and A. Hall. 2002. Rho GTPases in cell biology. *Nature.* 420:629–635. http://dx.doi.org/10.1038/nature01148

Fanti, Z., M.E. Martinez-Perez, and F.F. De-Miguel. 2011. NeuronGrowth, a software for automatic quantification of neurite and filopodial dynamics from time-lapse sequences of digital images. *Dev. Neurobiol.* 71:870–881. http://dx.doi.org/10.1002/dneu.20866

Gallo, G. 2006. RhoA-kinase coordinates F-actin organization and myosin II activity during semaphorin-3A-induced axon retraction. *J. Cell Sci.* 119:3413–3423. http://dx.doi.org/10.1242/jcs.03084

Gates, J., J.P. Mahaffey, S.L. Rogers, M. Emerson, E.M. Rogers, S.L. Sottile, D. Van Vactor, F.B. Gertler, and M. Peifer. 2007. Enabled plays key roles

in embryonic epithelial morphogenesis in *Drosophila*. *Development*. 134:2027–2039. http://dx.doi.org/10.1242/dev.02849

Gates, J., S.H. Nowotarski, H. Yin, J.P. Mahaffey, T. Bridges, C. Herrera, C.C. Homem, F. Janody, D.J. Montell, and M. Peifer. 2009. Enabled and Capping protein play important roles in shaping cell behavior during *Drosophila* oogenesis. *Dev. Biol.* 333:90–107. http://dx.doi.org/10.1016/j.ydbio.2009.06.030

Gertler, F.B., K. Niebuhr, M. Reinhard, J. Wehland, and P. Soriano. 1996. Mena, a relative of VASP and *Drosophila* Enabled, is implicated in the control of microfilament dynamics. *Cell*. 87:227–239. http://dx.doi.org/10.1016/S0092-8674(00)81341-0

Goode, B.L., and M.J. Eck. 2007. Mechanism and function of formins in the control of actin assembly. *Annu. Rev. Biochem.* 76:593–627. http://dx.doi.org/10.1146/annurev.biochem.75.103004.142647

Gupton, S.L., K. Eisenmann, A.S. Alberts, and C.M. Waterman-Storer. 2007. mDia2 regulates actin and focal adhesion dynamics and organization in the lamella for efficient epithelial cell migration. *J. Cell Sci.* 120:3475–3487. http://dx.doi.org/10.1242/jcs.006049

Hansen, S.D., and R.D. Mullins. 2010. VASP is a processive actin polymerase that requires monomeric actin for barbed end association. *J. Cell Biol.* 191:571–584. http://dx.doi.org/10.1083/jcb.201003014

Hodgson, L., P. Nalbant, F. Shen, and K. Hahn. 2006. Imaging and photobleach correction of Mero-CBD, sensor of endogenous Cdc42 activation. *Methods Enzymol.* 406:140–156.

Homem, C.C., and M. Peifer. 2008. Diaphanous regulates myosin and adherens junctions to control cell contractility and protrusive behavior during morphogenesis. *Development*. 135:1005–1018. http://dx.doi.org/10.1242/dev.016337

Homem, C.C.F., and M. Peifer. 2009. Exploring the roles of diaphanous and enabled activity in shaping the balance between filopodia and lamellipodia. *Mol. Biol. Cell*. 20:5138–5155. http://dx.doi.org/10.1091/mbc.E09-02-0144

Jaffe, A.B., and A. Hall. 2005. Rho GTPases: biochemistry and biology. *Annu. Rev. Cell Dev. Biol.* 21:247–269. http://dx.doi.org/10.1146/annurev.cellbio.21.020604.150721

Lizárraga, F., R. Poincloux, M. Romao, G. Montagnac, G. Le Dez, I. Bonne, G. Rigaill, G. Raposo, and P. Chavrier. 2009. Diaphanous-related formins are required for invadopodia formation and invasion of breast tumor cells. *Cancer Res.* 69:2792–2800. http://dx.doi.org/10.1158/0008-5472.CAN-08-3709

Loudon, R.P., L.D. Silver, H.F. Yee Jr., and G. Gallo. 2006. RhoA-kinase and myosin II are required for the maintenance of growth cone polarity and guidance by nerve growth factor. *J. Neurobiol.* 66:847–867. http://dx.doi.org/10.1002/neu.20258

Mayya, N., and V.T. Rijan. 1995. An efficient shape representation scheme using Voronoi skeletons. *Pattern Recognit. Lett.* 16:147–160. http://dx.doi.org/10.1016/0167-8655(94)00087-J

McKerracher, L., and H. Higuchi. 2006. Targeting Rho to stimulate repair after spinal cord injury. *J. Neurotrauma*. 23:309–317. http://dx.doi.org/10.1089/neu.2006.23.309

Meijering, E., M. Jacob, J.C.F. Sarria, P. Steiner, H. Hirling, and M. Unser. 2004. Design and validation of a tool for neurite tracing and analysis in fluorescence microscopy images. *Cytometry A*. 58A:167–176. http://dx.doi.org/10.1002/cyto.a.20022

Morse, B.S., S.M. Pizer, and A. Liu. 1994. Multiscale medial analysis of medical images. *Image Vis. Comput.* 12:327–338. http://dx.doi.org/10.1016/0262-8856(94)90057-4

Mueller, B.K., H. Mack, and N. Teusch. 2005. Rho kinase, a promising drug target for neurological disorders. *Nat. Rev. Drug Discov.* 4:387–398. http://dx.doi.org/10.1038/nrd1719

Peng, J., B.J. Wallar, A. Flanders, P.J. Swiatek, and A.S. Alberts. 2003. Disruption of the Diaphanous-related formin Drf1 gene encoding mDia1 reveals a role for Drf3 as an effector for Cdc42. *Curr. Biol.* 13:534–545. http://dx.doi.org/10.1016/S0960-9822(03)00170-2

Pertz, O., L. Hodgson, R.L. Klemke, and K.M. Hahn. 2006. Spatiotemporal dynamics of RhoA activity in migrating cells. *Nature*. 440:1069–1072. http://dx.doi.org/10.1038/nature04665

Philippar, U., E.T. Roussos, M. Oser, H. Yamaguchi, H.-D. Kim, S. Giampieri, Y. Wang, S. Goswami, J.B. Wyckoff, D.A. Lauffenburger, et al. 2008. A Mena invasion isoform potentiates EGF-induced carcinoma cell invasion and metastasis. *Dev. Cell*. 15:813–828. http://dx.doi.org/10.1016/j.devcel.2008.09.003

Qi, Y., J.K. Wang, M. McMillian, and D.M. Chikaraishi. 1997. Characterization of a CNS cell line, CAD, in which morphological differentiation is initiated by serum deprivation. *J. Neurosci.* 17:1217–1225.

Sarmiento, C., W. Wang, A. Dovas, H. Yamaguchi, M. Sidani, M. El-Sibai, V. Desmarais, H.A. Holman, S. Kitchen, J.M. Backer, et al. 2008. WASP family members and formin proteins coordinate regulation of cell protrusions in carcinoma cells. *J. Cell Biol.* 180:1245–1260. http://dx.doi.org/10.1083/jcb.200708123

Schirenbeck, A., T. Bretschneider, R. Arasada, M. Schleicher, and J. Faix. 2005. The Diaphanous-related formin dDia2 is required for the formation and maintenance of filopodia. *Nat. Cell Biol.* 7:619–625. http://dx.doi.org/10.1038/ncb1266

Sebök, A., N. Nusser, B. Debreceni, Z. Guo, M.F. Santos, J. Szeberenyi, and G. Tigyi. 1999. Different roles for RhoA during neurite initiation, elongation, and regeneration in PC12 cells. *J. Neurochem.* 73:949–960. http://dx.doi.org/10.1046/j.1471-4159.1999.0730949.x

Styner, M., G. Gerig, J. Lieberman, D. Jones, and D. Weinberger. 2003. Statistical shape analysis of neuroanatomical structures based on medial models. *Med. Image Anal.* 7:207–220. http://dx.doi.org/10.1016/S1361-8415(02)00110-X

Tek, H., and B.B. Kimia. 2003. Symmetry maps of free-form curve segments via wave propagation. *Int. J. Comput. Vis.* 54:35–81. http://dx.doi.org/10.1023/A:1023753317008

Woo, S., and T.M. Gomez. 2006. Rac1 and RhoA promote neurite outgrowth through formation and stabilization of growth cone point contacts. *J. Neurosci.* 26:1418–1428. http://dx.doi.org/10.1523/JNEUROSCI.4209-05.2006

Yang, C., L. Czech, S. Gerboth, S.-i. Kojima, G. Scita, and T. Svitkina. 2007. Novel roles of formin mDia2 in lamellipodia and filopodia formation in motile cells. *PLoS Biol.* 5:e317. http://dx.doi.org/10.1371/journal.pbio.0050317

Yuan, X.B., M. Jin, X. Xu, Y.Q. Song, C.P. Wu, M.M. Poo, and S. Duan. 2003. Signalling and crosstalk of Rho GTPases in mediating axon guidance. *Nat. Cell Biol.* 5:38–45. http://dx.doi.org/10.1038/ncb895